The Astrophysical Journal, 846:120 (25pp), 2017 September 10 https://doi.org/10.3847/1538-4357/aa8368

The KMOS Cluster Survey (KCS). I. The Fundamental Plane and the Formation Ages of Cluster Galaxies at Redshift $1.4 < Z < 1.6$*

Alessandra Beifiori[1,2], J. Trevor Mendel[1,2], Jeffrey C. C. Chan[1,2,3], Roberto P. Saglia[1,2], Ralf Bender[1,2], Michele Cappellari[4], Roger L. Davies[4], Audrey Galametz[1,2], Ryan C. W. Houghton[4], Laura J. Prichard[4], Russell Smith[5], John P. Stott[4,6], David J. Wilman[1,2], Ian J. Lewis[4], Ray Sharples[5], and Michael Wegner[1]

[1] Universitäts-Sternwarte München, Scheinerstraße 1, D-81679 München, Germany; beifiori@mpe.mpg.de
[2] Max-Planck-Institut für Extraterrestrische Physik, Giessenbachstraße 1, D-85748 Garching, Germany
[3] Department of Physics and Astronomy, University of California, Riverside, CA 92521, USA
[4] Sub-department of Astrophysics, Department of Physics, University of Oxford, Denys Wilkinson Building, Keble Road, Oxford OX1 3RH, UK
[5] Centre for Advanced Instrumentation, Department of Physics, Durham University, South Road, Durham DH1 3LE, UK
[6] Department of Physics, Lancaster University, Lancaster LA1 4 YB, UK

Received 2017 April 24; revised 2017 July 21; accepted 2017 July 30; published 2017 September 8

Abstract

We present the analysis of the fundamental plane (FP) for a sample of 19 massive red-sequence galaxies ($M_\star > 4 \times 10^{10}\, M_\odot$) in three known overdensities at $1.39 < z < 1.61$ from the K-band Multi-object Spectrograph (KMOS) Cluster Survey, a guaranteed-time program with spectroscopy from the KMOS at the VLT and imaging from the *Hubble Space Telescope*. As expected, we find that the FP zero-point in B band evolves with redshift, from the value 0.443 of Coma to -0.10 ± 0.09, -0.19 ± 0.05, and -0.29 ± 0.12 for our clusters at $z = 1.39$, $z = 1.46$, and $z = 1.61$, respectively. For the most massive galaxies ($\log M_\star / M_\odot > 11$) in our sample, we translate the FP zero-point evolution into a mass-to-light-ratio M/L evolution, finding $\Delta \log M/L_B = (-0.46 \pm 0.10)z$, $\Delta \log M/L_B = (-0.52 \pm 0.07)z$, to $\Delta \log M/L_B = (-0.55 \pm 0.10)z$, respectively. We assess the potential contribution of the galaxy structural and stellar velocity dispersion evolution to the evolution of the FP zero-point and find it to be ~6%–35% of the FP zero-point evolution. The rate of M/L evolution is consistent with galaxies evolving passively. Using single stellar population models, we find an average age of $2.33^{+0.86}_{-0.51}$ Gyr for the $\log M_\star / M_\odot > 11$ galaxies in our massive and virialized cluster at $z = 1.39$, $1.59^{+1.40}_{-0.62}$ Gyr in a massive but not virialized cluster at $z = 1.46$, and $1.20^{+1.03}_{-0.47}$ Gyr in a protocluster at $z = 1.61$. After accounting for the difference in the age of the universe between redshifts, the ages of the galaxies in the three overdensities are consistent within the errors, with possibly a weak suggestion that galaxies in the most evolved structure are older.

Key words: galaxies: clusters: general – galaxies: elliptical and lenticular, cD – galaxies: evolution – galaxies: formation – galaxies: high-redshift – galaxies: kinematics and dynamics

1. Introduction

Early-type galaxies in the local universe lie along a tight relation, the "fundamental plane" (FP, e.g., Djorgovski & Davis 1987; Dressler et al. 1987), connecting their surface brightness within the effective radius $\langle I_e \rangle$, effective radius R_e, and velocity dispersion within the effective radius σ_e. The FP is tilted with respect to the virial prediction; the tilt is related to the change of the mass-to-light (M/L) ratio with galaxy luminosity, which is due to a contribution of variations of the galaxy stellar populations, dark matter fractions, and non-homology (e.g., Bender et al. 1992; Renzini & Ciotti 1993; Jørgensen et al. 1996; Cappellari et al. 2006, 2013b; Renzini 2006; Scott et al. 2015; Cappellari 2016). While there is still debate on whether the coefficients of the FP remain constant up to $z \sim 1$ (see Holden et al. 2010; Saglia et al. 2010a; Jørgensen & Chiboucas 2013), there is a clear consensus about the variation of its zero-point with redshift. The zero-point can vary as a result of evolving M/L (Faber et al. 1987) caused by the change in galaxy luminosity that is due to the younger stellar population at high-z (e.g., van Dokkum & Franx 1996; Bender et al. 1998; Kelson et al. 2000; Gebhardt et al. 2003; Wuyts et al. 2004; Holden et al. 2005; di Serego Alighieri et al. 2005; Jørgensen et al. 2006; van Dokkum & van der Marel 2007; Holden et al. 2010; Toft et al. 2012; Bezanson et al. 2013; Jørgensen et al. 2014); some contribution is also expected from the galaxy structural evolution with redshift (e.g., Saglia et al. 2010a, 2016).

Several papers have shown that intermediate- and high-redshift passive galaxies have smaller sizes (e.g., Trujillo et al. 2007; Houghton et al. 2012; Newman et al. 2012; Beifiori et al. 2014; van der Wel et al. 2014; Chan et al. 2016) and higher stellar velocity dispersions (e.g., Cappellari et al. 2009; Cenarro & Trujillo 2009; van Dokkum et al. 2009; van de Sande et al. 2013; Belli et al. 2014a, 2014b, 2015) than their local counterparts of the same mass or fixed cumulative number density (e.g., Brammer et al. 2011; Papovich et al. 2011; Muzzin et al. 2013; Patel et al. 2013; van Dokkum et al. 2013).

Several authors also suggested that environmental effects may accelerate the size evolution in clusters compared to the field at $z > 1.4$, finding that galaxies in clusters are larger than the field galaxies at the same redshift (e.g., Lani et al. 2013; Strazzullo et al. 2013; Delaye et al. 2014, Chan et al. 2017, but see also Saracco et al. 2014 and Newman et al. 2014 for different results). In the local universe there are instead negligible differences between the mean galaxy sizes in

---

* Based on observations obtained at the Very Large Telescope (VLT) of the European Southern Observatory (ESO), Paranal, Chile (ESO program IDs: 092.A-0210(A); 093.A-0051(A/B); 094.A-0578(A); 095.A-0137(A); 096.A0189(A); 097.A-0332(A). This work is further based on observations taken by the CANDELS Multi-cycle Treasury Program with the NASA/ESA *HST*, which is operated by the Association of Universities for Research in Astronomy, Inc., under NASA contract NAS 5-26555.

different environments (e.g., Cappellari 2013; Huertas-Company et al. 2013).

The rate of the M/L evolution is described by $\Delta \log M/L \propto z$, as seen from both samples of massive cluster (e.g., van Dokkum & Franx 1996; Barr et al. 2006; Jørgensen et al. 2006; Holden et al. 2010; Saglia et al. 2010a) and field galaxies (e.g., Treu et al. 2005; van der Wel et al. 2005; Saglia et al. 2010a; van de Sande et al. 2014). By fitting passively evolving simple stellar population models, the M/L evolution can be translated into a formation redshift corresponding to the epoch of the last major star formation episode (e.g., Tinsley & Gunn 1976). This technique assumes a uniform population across all the galaxies, it assumes that the single stellar population model approximation holds, and that high-redshift clusters evolve into a reference low-redshift cluster without any additional star formation, merging, or quenching of star formation.

Following this method, some authors found that the stellar populations in galaxies in clusters at $z \leqslant 1$ are older than in field galaxies (e.g., Gebhardt et al. 2003; van Dokkum & van der Marel 2007; Saglia et al. 2010a), suggesting an accelerated evolution of passive galaxies in dense environments. An age difference between galaxies in clusters and field could be expected, considering that clusters are formed in the highest density regions of the universe, which collapse first. Conversely, other authors (e.g., Treu et al. 2005; van der Wel et al. 2005; di Serego Alighieri et al 2006; Renzini 2006) found that the stellar mass, rather than environment, is the best predictor of galaxy ages, with massive galaxies being older. Further work on the star formation history of massive galaxies from the α/Fe abundance in the local universe suggested that the star formation timescales are short and that more massive galaxies are older than those at lower mass, with age differences between clusters and field galaxies in some case (e.g., Thomas et al. 2005) and similar ages in other cases (e.g., Thomas et al. 2010). The latter is in agreement with the lack of significant difference in M/L as measured from detailed dynamical models (Cappellari et al. 2006, 2013b).

The advent of new IR spectrographs at the ESO Very Large Telescope (VLT) and the Keck Observatory recently enabled the observation of rest-frame optical spectra for an increasingly larger number of passive galaxies in the field at $z > 1.3$ (e.g., van de Sande et al. 2011; van de Sande et al. 2013; Mendel et al. 2015; J. T. Mendel et al. 2017, in preparation at VLT, and Belli et al. 2015, 2017 at Keck), some of which were also used to constrain the galaxies' formation redshift using the FP (e.g., van de Sande et al. 2014). At $z > 1.3$, differences in the kinematics and formation ages of passive galaxies in different environments are currently almost unexplored. At these redshifts, we expect to have more constraints on age differences than in the local universe, where a 2 Gyr difference in a population of ~8–10 Gyr would be challenging to constrain.

In this paper we investigate the evolution of the FP of massive and passive galaxies in dense environments at redshift $1.39 < z < 1.61$ as a part of the KMOS Cluster Survey (KCS, Davies et al. 2015, R. J. Davies et al. 2017, in preparation). KCS is a guaranteed-time observation (GTO) program mapping the red sequence of cluster galaxies at $1.39 < z < 1.8$ with the *K*-band Multi-object Spectrograph (KMOS, Sharples et al. 2012, 2014) at the ESO VLT. The multiplexing and near-infrared capabilities of KMOS allow us to simultaneously observe ⩾20 galaxies per overdensity, and map the rest-frame optical absorption features commonly studied in the local universe (e.g., Bender 1990; Bender et al. 1994) using the KMOS *YJ* band with a resolution of $R \sim 3500$. The combination of our KMOS data with the available *Hubble Space Telescope* (*HST*) imaging allows us to trace the evolution of the FP of quiescent galaxies in dense environments at $z \geqslant 1.39$ with one of the largest samples to date.

The paper is organized as follows. The KCS survey, the cluster and galaxy sample, *HST* imaging and KMOS spectroscopic data are presented in Section 2. Measurements of velocity dispersions and structural parameters are described in Section 3. The local and intermediate-redshift samples used as reference are described in Section 4. The results are presented in Section 5 and discussed in Section 6. The paper concludes with Section 7. Additional information on the derivation of the kinematics, the selection functions for our sample, and the effect of different stellar population models and metallicity assumptions in our analysis are provided in Appendices A–C.

Throughout the paper we assume a standard cosmology with $H_0 = 70\,\mathrm{km\,s^{-1}\,Mpc^{-1}}$, $\Omega_\mathrm{m} = 0.3$, and $\Omega_\Lambda = 0.7$. For this cosmology, 1″ corresponds to 8.43 kpc, 8.45 kpc, and 8.47 kpc at the mean redshift of our overdensities (XMMU J2235.3-2557 at $z = 1.39$, XMMXCS J2215.9-1738 at $z = 1.46$, and Cl 0332-2742 at $z = 1.61$), respectively. All magnitudes are in the AB photometric system (Oke & Gunn 1983). Throughout the paper we use the term "overdensity" and "cluster" interchangeably (but we highlight when the distinction is astrophysically meaningful).

2. Sample and Data

2.1. The KMOS Cluster Survey

The KCS is a 30-night KMOS GTO program performing deep absorption-line spectroscopy in *four main overdensities* at $1.39 < z < 1.8$ and *one lower-priority overdensity* at $z = 1.04$ to bridge our high-redshift observations with the local sample. The sample includes RCS 234526-3632.6 at $z = 1.04$ (Meyers et al. 2012, hereafter RCS2345), XMMU J2235.3-2557 at $z = 1.39$ (Mullis et al. 2005; Rosati et al. 2009, hereafter XMM2235), XMMXCS J2215.9-1738 at $z = 1.46$ (Stanford et al. 2006; Hilton et al. 2007, 2009, 2010, hereafter XMM2215), Cl 0332-2742 at $z = 1.61$ (Castellano et al. 2007; Kurk et al. 2009, hereafter Cl0332), and JKCS 041 at $z = 1.8$ (Andreon et al. 2014; Newman et al. 2014). We observed ⩾20 galaxies in the field of each overdensity with the aim of studying the evolution of kinematics and stellar populations in dense environments at high redshift.

The overdensities were selected to have a significant amount of archival data, spanning from multiband *HST* photometry to deep ground-based imaging, and a large number of spectroscopically confirmed members to maximize the galaxy selection efficiency, concentrating on objects with lower contamination from strong sky emission or telluric absorption.

The KMOS patrol field of 7$'\!.$2 diameter covers the extent of the core of our overdensities on the sky (~3 Mpc at the redshift of our overdensities). The integral-field unit (IFU) dimensions, 2$''\!.$8 × 2$''\!.$8 (~24 × 24 kpc at the redshift of our overdensities), are generally larger than the size of passive galaxies at $z \sim 1.5$ in most of the cases, allowing us to recover their total flux within an IFU. Each IFU has 0$''\!.$2 × 0$''\!.$2 spatial pixels.

During the ESO periods P92-P97, KCS targeted a total of 106 galaxies from our main cluster sample at $1.39 < z < 1.8$, including 20–40 galaxies in each structure. Of those, 67 galaxies were red-sequence selected, and were observed with exposure times of ∼15–20 hr on source and seeing $<1''$. This represents one of the largest samples of passive galaxies homogeneously observed and measured in *dense environments* at $z > 1.3$. During the same ESO periods, we also observed ∼20 galaxies part of our lower-priority target RCS2345 with exposure time of ∼9 hr on source.

2.2. The Sample of Overdensities

In this paper we present the analysis of three overdensities in KCS: XMM2235, XMM2215, and Cl0332, whose general properties we summarize below.

XMM2235 is a very massive ($M_{200} = 7.7^{+4.4}_{-3.1} \times 10^{14}\ h^{-1}\ M_{\odot}$, Stott et al. 2010) and virialized cluster (e.g., Rosati et al. 2009; Stott et al. 2010; Jee et al. 2011) that was discovered by Mullis et al. (2005). This cluster has a centrally peaked X-ray surface brightness profile, suggesting a dynamically relaxed state (Rosati et al. 2009). Analysis of stacked spectra (e.g., Rosati et al. 2009) and colors and the scatter of the red sequence (e.g., Lidman et al. 2008) indicated that massive ($\log M_{\star}/M_{\odot} > 11$) galaxies in the core have high formation redshift ($z > 3$–4). Further studies of the luminosity function (Strazzullo et al. 2010) indicate an established high-mass population, suggesting that this cluster is already at an evolved mass-assembly stage. Its central regions (within ∼200 kpc) show no evidence of star formation (e.g., Strazzullo et al. 2010; Bauer et al. 2011), and generally, all massive galaxies have low star formation rates (e.g., Grützbauch et al. 2012). In the outskirts instead, many galaxies show signatures of star formation as determined from H_{α} narrow-band imaging (e.g., Bauer et al. 2011; Grützbauch et al. 2012).

XMM2215, discovered by Stanford et al. (2006), is a massive overdensity ($M_{200} = 2.1^{+1.9}_{-0.8} \times 10^{14}\ h^{-1}\ M_{\odot}$, Stott et al. 2010), with extended X-ray emission from the hot gas, suggesting that the cluster is in a relatively advanced evolutionary stage. However, the cluster is unlikely to be fully virialized (e.g., Ma et al. 2015), as the galaxy velocity distribution is bimodal (e.g., Hilton et al. 2007, 2010) and there is no clear brightest cluster galaxy (BCG, see Hilton et al. 2009; Stott et al. 2010). The nominal BCG is a spectroscopically confirmed member at ∼300 kpc from the X-ray centroid and only marginally brighter than other cluster members. The red sequence of XMM2215 is made by relatively faint and low-mass objects and has a scatter significantly larger than that of local clusters or XMM2235 (e.g., Hilton et al. 2009). From the scatter and the intercept of the red sequence, Hilton et al. (2009) derived a galaxy formation redshift in the range $z_{\rm f} \sim 3$–5. A significant amount of red-sequence galaxies show some level of star formation, with [O$_{\rm II}$] emission in their observed spectra (e.g., Hilton et al. 2009, 2010) or via narrow-band imaging (Hayashi et al. 2010, 2011, 2014). Some galaxies in the cluster core show a significant amount of obscured star formation with substantial emission at 24 μm (e.g., Hilton et al. 2010) and in submillimeter bands (e.g., Ma et al. 2015; Stach et al. 2017), and there are also a significant number of AGNs (Hayashi et al. 2011). Moreover, the lack of CO emission in the very center of the overdensity also provided some constraints on the possible quenching mechanism that galaxies in the cluster experienced (e.g., Hayashi et al. 2017).

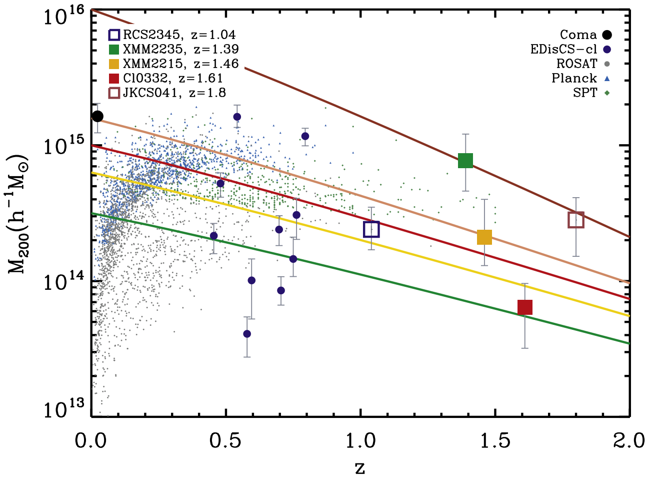

Figure 1. Cluster mass (M_{200}) vs. redshift for our full sample of KCS clusters from $1.04 < z < 1.8$. The green, orange, and red filled squares are the clusters described in this paper, XMM2235, XMM2215, and Cl0332. Cluster masses were derived from X-ray data or from the cluster velocity dispersion, as tabulated in Stott et al. (2010) and Kurk et al. (2009), respectively. The blue and brown open squares show the two additional overdensities from our survey, which will be discussed in subsequent papers, RCS2345 at $z = 1.04$ in blue (M_{200} from the weak-lensing analysis of Jee et al. 2011) and JKCS 041 at $z = 1.8$ in brown (M_{200} from X-ray analysis of Andreon et al. 2014). We also show the M_{200} for our local reference cluster Coma (Łokas & Mamon 2003) and for the subsample of EDisCS clusters and groups of Saglia et al. (2010a), which represents our intermediate-redshift reference (see Section 4 for details). Clusters found through wide-angle surveys, such as *ROSAT* (Piffaretti et al. 2011), *Planck* (Planck Collaboration et al. 2016), and SPT (Bleem et al. 2015), are also shown. For comparison we plot the mass accretion history of halos of different initial masses $M_{\rm in}$ derived with the COncentration–Mass relation and Mass Accretion History code (COMMAH; Correa et al. 2015a, 2015b, 2015c) with continuous lines ($\log M_{\rm in}/M_{\odot} = 16$ in brown, $\log M_{\rm in}/M_{\odot} = 15.2$ in pink, $\log M_{\rm in}/M_{\odot} = 15$ in red, $\log M_{\rm in}/M_{\odot} = 14.8$ in yellow, and $\log M_{\rm in}/M_{\odot} = 14.5$ in green).

Cl0332 was first identified as an overdensity using photometric redshifts (Castellano et al. 2007) and was confirmed by the Galaxy Mass Assembly ultra-deep Spectroscopic Survey (GMASS, Kurk et al. 2013), which targeted photometric redshift-selected galaxies ($z_{\rm phot} > 1.4$) in the Great Observatories Origins Survey (GOODS) Southern field (Giavalisco et al. 2004). The mass of this overdensity ranges from $M_{200} = 6.4^{+0.3}_{-0.3} \times 10^{13}\ h^{-1}\ M_{\odot}$ as measured from the cluster velocity dispersion, assuming the structure is virialized (Kurk et al. 2009, see Figure 1), to $M_{200} = 1.2 \times 10^{14}\ h^{-1}\ M_{\odot}$ as measured summing the mass of the X-ray groups in the field (e.g., Finoguenov et al. 2015). The members show a bimodal distribution in velocity, suggesting that the structure is mostly formed by two main groups with no clear evidence of spatial separation (e.g., Kurk et al. 2009). There is no obvious X-ray emission throughout the full structure (e.g., Kurk et al. 2009; Finoguenov et al. 2015), and the low signal-to-noise ratio (S/N) does not permit a proper separation from the foreground sources; most of the X-ray emission comes from the most massive group in the system discussed in Tanaka et al. (2013). These findings suggest that Cl0332 is likely a cluster in formation. Nevertheless, Cl0332 shows a clear red sequence in the color–magnitude diagram. The analysis of the stellar population from stacked spectra shows that galaxies have a relatively young age, a low specific star formation rate, and significant dust extinction (Cimatti et al. 2008; Kurk et al. 2009).

Figure 1 shows the cluster masses as a function of redshift for the KCS sample described in this paper (XMM2235, XMM2215, and Cl0332). For reference, we also show the two additional overdensities that are part of the full KCS sample, JKC S041 and RCS2345. The FP of JKC S041 will be presented in L. J. Prichard et al. 2017, in preparation.

As a local reference we use the Coma cluster (see also Section 4). Following the prescriptions of Hu & Kravtsov (2003), we rescale the mass within the virial radius of Coma from Łokas & Mamon (2003) to the mass within the radius R_{200}—inside which the average mass density is 200 times the critical density of the universe—finding $M_{200} = (1.6 \pm 0.4) \times 10^{15}\ h^{-1}\ M_{\odot}$. For this calculation we used a halo concentration parameter as described by Bullock et al. (2001).

Our intermediate-redshift reference is a subsample of the EDisCS clusters and groups (thereafter called "EDisCS-cl") used in the FP study of Saglia et al. (2010a), for which *HST* imaging is available (see also Section 4). Their M_{200} was calculated from their tabulated cluster stellar velocity dispersion (see Table 4 of Saglia et al. 2010a) following the prescription of Carlberg et al. (1997).

For comparison, we show public catalogs of clusters from other wide-angle cluster surveys, including *ROSAT* (Piffaretti et al. 2011), *Planck* (Planck Collaboration et al. 2016), and SPT (Bleem et al. 2015), whose masses M_{500} were converted into M_{200} following the prescriptions of Hu & Kravtsov (2003) with a halo concentration parameter of 5.

We overplot models for the growth of cluster mass with time, based on the COncentration–Mass relation and Mass Accretion History (COMMAH; Correa et al. 2015a, 2015b, 2015c) code, which uses an analytic model to generate halo mass accretion rates for a variety of redshifts and cluster masses.

According to these predictions, the two most massive overdensities in KCS, XMM2235 and JKCS 041, will evolve into clusters with a M_{200} higher than that measured for our local comparison cluster Coma. Moreover, only two clusters from the EDisCS-cl sample are in a mass range similar to the most massive overdensities in KCS.

2.3. Target Selection

2.3.1. Imaging

Archival imaging from the *HST* Advanced Camera for Survey (ACS) and the Wide Field Camera 3 (WFC3) is available for our sample (e.g., Chan et al. 2016; Chan et al. 2017) as well as photometric data from the ground.

For XMM2235, ACS data are available from program GTO-10698 and GO-10496, and WFC3 data are available from program GO/DD-12051; for XMM2215, ACS data come from the program GO-10496. All the *HST* data were processed as described by Chan et al. (2016) and Chan et al. (2017), using `ASTRODRIZZLE` (Gonzaga et al. 2012). For this paper we used the ACS/$z_{\rm F850lp}$ and WFC3 $Y_{\rm F105w}$ and $H_{\rm F160w}$ bands for the two clusters; see Chan et al. (2016) and Chan et al. (2017) for more details on the available bands. For XMM2215, we also used a *J*-band image from the Multi-object InfraRed Camera and Spectrograph (MOIRCS) at Subaru Telescope (Hilton et al. 2009) with a seeing FWHM ~ 0$''$.6.

The *HST* (or MOIRCS) imaging of XMM2235 and XMM2215 has a small field of view, which could bias our absolute astrometric solutions. Therefore we applied to our WFC3 and MOIRCS images the same astrometry of the *Ks*-band HAWK-I images available for the two clusters (Lidman et al. 2008, 2013, and C. Lidman 2017, private communication),[7] which has a larger field of view.

Source catalogs were produced using SExtractor (Bertin & Arnouts 1996), with the reddest image, or with the image with the higher resolution used for detection. We flagged stars with a star-galaxy classification `class_star` $\geqslant 0.9$. We measured both `MAG_AUTO` and aperture magnitudes within an aperture of diameter 1$''$, which were corrected for Galactic reddening in the direction of the cluster using the values given by the the NASA Extragalactic Database extinction law calculator,[8] which is based on the maps by Schlafly & Finkbeiner (2011). The apertures are larger than the point-spread function (PSF) of our images, and we expect the aperture size not to have an impact in the derived magnitudes. In the final catalog of XMM2215, we included only galaxies with photometric redshift in the range $1.27 < z < 1.65$ from Hilton et al. (2009) or with available spectroscopic redshift from the same paper. The galaxy IDs in Table 1 come from our $H_{\rm F160w}$ catalog for XMM2235 and from the $z_{\rm F850lp}$ catalog for XMM2215 (see also Chan et al. 2017).

For Cl0332, we used public ACS and WFC3 mosaics in the $I_{\rm F814w}$ and $J_{\rm F125w}$ bands, respectively, from the Cosmic Assembly Near-IR Deep Extragalactic Legacy Survey (CANDELS; Grogin et al. 2011; Koekemoer et al. 2011) as provided by the 3DHST survey (Skelton et al. 2014) as well as the public catalog in the GOODS-S field (Guo et al. 2013; Skelton et al. 2014; Momcheva et al. 2016). The magnitudes provided in these catalogs are total PSF-matched magnitudes. We used these when we needed total magnitudes, whereas to derive aperture magnitudes, we followed Equation (3) of Skelton et al. (2014) to rescale the provided total magnitudes to the original 0$''$.7 aperture magnitudes and their errors. The use of different apertures between Skelton et al. (2014) and Chan et al. (2016) does not affect our selection because effective radii of most galaxies in our sample are smaller than the aperture size. Magnitudes in Skelton et al. (2014) are extinction corrected using the maps by Schlafly & Finkbeiner (2011). We selected potential cluster members in the GOODS-S field as those within ± 3000 km s^{-1} of the systemic redshift using the best spectroscopic, grism, or photometric estimation from 3DHST[9] (`z_best`, Momcheva et al. 2016) and within a region covering the KMOS field of view (i.e., 7.2 arcmin diameter). This includes both the upper part of the Kurk et al. (2009) structure and the Tanaka et al. (2013) group. In Chan et al. (2017), we derive our own SExtractor catalog of the WFC3/$H_{\rm F160w}$ CANDELS images; the IDs we provide in Table 1 come from that catalog.

2.3.2. Color–Magnitude Diagrams (CMD)

In Figure 2 we show the resulting color–magnitude diagram of the three overdensities. The red-sequence relations are fitted from the CMDs (solid lines), and their scatter is measured by marginalizing over the magnitude to obtain the distribution of galaxies. The dashed lines in the CMDs correspond to the 2σ scatter derived from a Gaussian fit of this distribution. In

---

[7] Based on data products from observations made with ESO Telescopes at the La Silla Paranal Observatory under program ID 060.A-9284(H).

[8] http://ned.ipac.caltech.edu/help/extinction_law_calc.html

[9] With some exceptions for objects with uncertain spectroscopic redshifts within our field of view.

Table 1
Properties of the Galaxies in XMM2235, XMM2215, and Cl0332

ID	R.A. (J2000)	Decl. (J2000)	Redshift	$(z - H)$	H mag	$\log\langle I_{\rm e}\rangle/(L_\odot\ {\rm pc}^{-2})$	$R_{\rm e}$ kpc	n	q	$\sigma_{\rm e}$ km s^{-1}	$\log M_\star/M_\odot$	$\log M_{\rm dyn}/M_\odot$
352	338.836332	−25.962342	1.3747	1.92	20.40	3.60 ± 0.15	1.97 ± 0.34	2.47 ± 0.24	0.64 ± 0.02	223.21 ± 52.92	11.23 ± 0.07	11.20 ± 0.22
296	338.840083	−25.957082	1.3793	1.38	21.53	3.33 ± 0.19	2.39 ± 0.52	0.95 ± 0.10	0.57 ± 0.02	308.40 ± 77.28	10.53 ± 0.05	11.63 ± 0.24
407	338.836328	−25.960471	1.3848	1.91	20.46	3.27 ± 0.30	3.94 ± 1.36	6.73 ± 1.05	0.66 ± 0.03	206.73 ± 50.36	11.24 ± 0.07	11.23 ± 0.26
220	338.845102	−25.940250	1.3902	1.69	21.52	3.37 ± 0.28	2.43 ± 0.79	5.15 ± 0.75	0.75 ± 0.04	180.67 ± 50.21	10.82 ± 0.06	10.98 ± 0.28
36	338.829552	−25.974256	1.3919	1.77	21.11	3.18 ± 0.28	3.45 ± 1.11	4.17 ± 0.64	0.79 ± 0.04	163.14 ± 30.85	11.04 ± 0.08	11.09 ± 0.22
576	338.841546	−25.949133	1.3937	1.80	21.02	3.93 ± 0.08	1.41 ± 0.13	2.76 ± 0.14	0.35 ± 0.01	376.71 ± 42.49	11.01 ± 0.08	11.50 ± 0.11
170	338.836838	−25.961102	1.3949	1.96	19.56	2.55 ± 0.70	13.51 ± 10.84	3.66 ± 1.22	0.62 ± 0.10	366.59 ± 43.65	11.82 ± 0.07	12.41 ± 0.36
433	338.829397	−25.964279	1.3951	1.91	21.41	3.07 ± 0.43	3.41 ± 1.70	5.61 ± 1.08	0.71 ± 0.05	232.28 ± 46.95	10.95 ± 0.07	11.33 ± 0.28
637	338.844880	−25.951640	1.3966	1.49	21.36	3.92 ± 0.08	1.35 ± 0.12	2.78 ± 0.16	0.77 ± 0.01	175.32 ± 66.00	10.69 ± 0.05	10.81 ± 0.33
ID	R.A.	Decl.	Redshift	$(z - J)$	J mag	$\log\langle I_{\rm e}\rangle/(L_\odot\ {\rm pc}^{-2})$	$R_{\rm e}$ kpc	n	q	$\sigma_{\rm e}$ km s^{-1}	$\log M_\star/M_\odot$	$\log M_{\rm dyn}/M_\odot$
864	333.996028	−17.634061	1.4505	1.58	21.97	3.58 ± 0.58	1.63 ± 1.09	2.01 ± 0.97	0.56 ± 0.09	182.56 ± 48.51	11.13 ± 0.10	10.96 ± 0.37
912	333.999518	−17.633135	1.4507	1.31	22.23	4.26 ± 0.20	0.73 ± 0.17	2.70 ± 0.48	0.62 ± 0.03	245.49 ± 77.49	10.76 ± 0.08	10.84 ± 0.29
1006	333.984149	−17.630537	1.4559	1.40	21.52	4.13 ± 0.25	1.27 ± 0.37	4.65 ± 1.06	0.30 ± 0.02	296.22 ± 58.11	11.11 ± 0.08	11.16 ± 0.21
710	333.983600	−17.639072	1.4587	1.38	22.41	3.60 ± 0.58	1.62 ± 1.09	2.92 ± 1.41	0.41 ± 0.07	294.19 ± 77.80	10.87 ± 0.08	11.33 ± 0.37
615	334.013234	−17.641575	1.4652	1.33	21.52	3.00 ± 0.18	4.84 ± 1.03	3.86 ± 1.89	0.60 ± 0.04	214.45 ± 65.13	11.03 ± 0.12	11.49 ± 0.28
781	333.993745	−17.636265	1.4703	1.41	21.69	3.34 ± 0.38	2.23 ± 0.99	0.78 ± 0.47	0.52 ± 0.11	198.18 ± 79.27	10.98 ± 0.08	11.22 ± 0.40
ID	R.A.	Decl.	Redshift	$(I - J)$	J mag	$\log\langle I_{\rm e}\rangle/(L_\odot\ {\rm pc}^{-2})$	$R_{\rm e}$ kpc	n	q	$\sigma_{\rm e}$ km s^{-1}	$\log M_\star/M_\odot$	$\log M_{\rm dyn}/M_\odot$
12177	53.052200	−27.774770	1.6078	2.42	21.63	3.68 ± 0.11	2.01 ± 0.23	1.62 ± 0.20	0.54 ± 0.02	318.46 ± 131.15	11.13 ± 0.12	11.55 ± 0.36
11827	53.044943	−27.774395	1.6102	2.52	20.93	2.90 ± 0.26	6.76 ± 2.01	2.33 ± 0.42	0.59 ± 0.05	227.67 ± 87.09	11.49 ± 0.07	11.76 ± 0.36
21853	53.062822	−27.726461	1.6110	2.12	21.37	3.97 ± 0.07	1.69 ± 0.11	3.38 ± 0.22	0.95 ± 0.02	212.09 ± 64.22	11.13 ± 0.13	11.05 ± 0.26
25972	53.104571	−27.705422	1.6136	2.47	21.81	3.65 ± 0.11	1.93 ± 0.22	2.88 ± 0.35	0.90 ± 0.03	209.87 ± 86.64	11.07 ± 0.10	11.12 ± 0.36

Note. Galaxy IDs for XMM2235 and Cl0332 come from our $H_{\rm F160w}$ catalogs (e.g., Chan et al. 2017), whereas for XMM2215, they come from the $z_{\rm F850lp}$ catalog. Galaxies in clusters are listed in increasing redshift order matching that of Figure 3. For XMM2235, the H-band corresponds to $H_{\rm F160w}$, whereas the $(z - H)$ color corresponds to $(z_{\rm F850lp} - H_{\rm F160w})$. For XMM2215, J corresponds to $J_{\rm MOIRCS}$, whereas the $(z - J)$ color corresponds to $(z_{\rm F850lp} - J_{\rm MOIRCS})$. For Cl0332, J band is $J_{\rm F125W}$ and $(I - J)$ corresponds to $(I_{\rm F814W} - J_{\rm F125W})$, see the CMDs in Figure 2. Magnitude and colors are extinction corrected. The surface brightness within the effective radius $\log\langle I_{\rm e}\rangle$ is in rest-frame B band. $R_{\rm e}$ is the circularized effective radius, n is the Sérsic index, q is the axis ratio, and $\sigma_{\rm e}$ is the stellar velocity dispersions within $R_{\rm e}$. Only galaxies for which we measured the stellar velocity dispersion, the "dispersion sample," are listed here. We remind the reader that with our cosmology, $1''$ corresponds to 8.43 kpc, 8.45 kpc, and 8.47 kpc at the mean redshift of our overdensities ($z = 1.39$, $z = 1.46$, and $z = 1.61$), respectively.

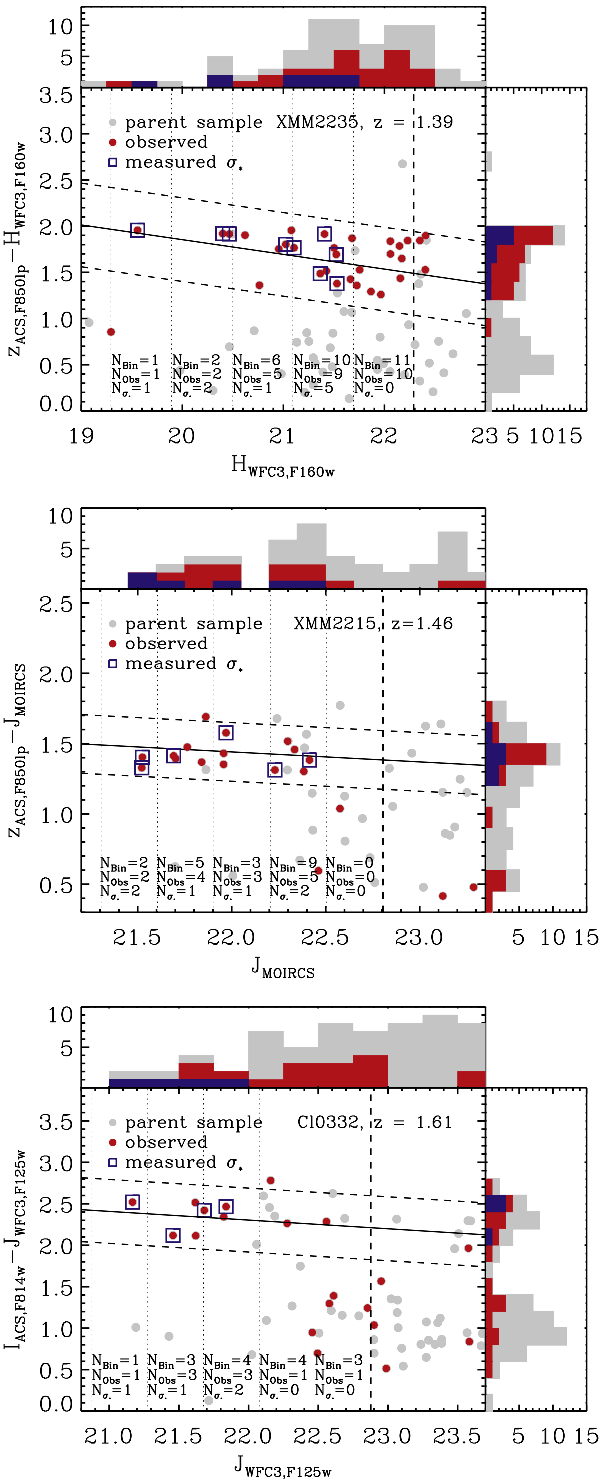

Figure 2. CMDs showing our parent sample (gray filled circles), the galaxies observed by KCS (red filled circles), and the galaxies for which we could derive stellar velocity dispersions (blue open squares), our dispersion sample, see Section 3.3. Black continuous lines are the best-fit red sequences, and black dashed lines show their 2σ scatter. Vertical dashed lines show the magnitude cut used in our completeness analysis (see Appendix B), $J_{F140w} < 22.5$, rescaled to the band used in the CMD. Vertical dotted lines show the magnitude bins used to evaluate the selection functions for our sample (see Appendix B), with the numbers of objects per bin—within the red sequence and our magnitude cut—shown at the bottom ($N_{\rm Bin}$), as well as objects observed with KMOS ($N_{\rm Obs}$) and for which we derived stellar velocity dispersion ($N_{\sigma_\star}$). Histograms show the distribution of colors and magnitudes for the three samples.

Table 1 we give the colors and magnitudes used in the CMDs only for the galaxies for which we measure stellar velocity dispersion (see Section 3.3); hereafter we refer to this as the dispersion sample.

Passive galaxies for the KMOS observations were selected to be within 2σ from the fitted red sequence of each cluster, to lie within both the ACS and WFC3 fields of view (when available at the time of the KMOS observations, see Chan et al. 2017 for the new WFC3 data collected after the KMOS observations), and to be bright. We prioritized bright objects with public spectroscopic redshifts when available in the red sequence of the CMDs, then objects in the red sequence with no redshift information, and finally included lower-priority fillers, either from faint red sequence objects or from the blue cloud to target emission lines. The latter will be described in a forthcoming paper (J. P. Stott et al. 2017, in preparation).

In the following, we apply a magnitude limit of $J_{\rm F140W} < 22.5$ to identify bright objects in our analysis, below which only fillers were included in our allocations. The actual value of the magnitude limit used in each of our samples in Figure 2 was derived by applying a color term to this threshold in $J_{\rm F140W}$ band to match the band used in the CMD; the color terms were obtained from Maraston (2005) simple stellar population models with an age >1 Gyr. Based on the simulations described in Chan et al. (2016) and Chan et al. (2017) within our magnitude limit we detect 93% of the objects in XMM2235, 98% in XMM2215, and 99% in Cl0332.

With a target selection based only on the red sequence, we would expect a number of interlopers, in particular at faint magnitudes. The number of possible foreground or background interlopers can be estimated by comparing the number of objects in the red sequence of our overdensities with the number of objects we find from constructing a CMD with field data in the same bands of our overdensities. We used photometric catalogs from the CANDELS/3DHST deep fields (Skelton et al. 2014; Momcheva et al. 2016), excluding the GOODS-S field because it is where one of our overdensities reside. We compared, per bin of magnitude, the number of objects in the red sequence of our overdensities to the number of objects of the red sequence found from constructing a CMD with the same band and data from the CANDELS/3DHST deep fields. The estimated number of interlopers were then rescaled by the ratio between the area of our observations and the area covered by CANDELS/3DHST in the bands of our CMDs. Our estimates are conservative because we assume that there are no overdensities in the CANDELS/3DHST deep fields.

Based on this comparison, we do not expect to find interlopers in the bright part of the red sequence ($H_{\rm F160w} < 20.5$) for XMM2235; moreover, at these bright magnitudes, our selection includes galaxies with prior spectroscopic redshifts from the literature. At fainter magnitudes ($21.7 < H_{\rm F160w} < 22.3$), where we also lack spectroscopic redshifts, the number of interlopers increases up to 50%. For XMM2215, we expect the number of interlopers to vary from 10% at bright magnitudes ($J_{\rm MOIRCS} < 21.9$) to ~30% in the faintest magnitude bin we targeted ($22.2 < J_{\rm MOIRCS} < 22.5$). At the faintest magnitude, the actual effect of the contamination by interlopers was significantly minimized by the the additional information about the photometric or spectroscopic redshift of the galaxies. For Cl0332, contamination can be more serious, more than 80% of the brighter galaxies ($J_{\rm F125w} < 21.68$) could be interlopers. This effect is particularly enhanced for this cluster given the lower number of objects in the red sequence. The availability of prior information about the galaxy redshifts significantly improved our target selection.

In Chan et al. (2017) we use new data collected after the KMOS observations, and construct two-color diagrams (*UVR* and *UVJ* rest-frame colors) to show that it is entirely unclear whether some of the faint objects in XMM2235 and XMM2215 are very dusty star-forming objects entering the red sequence or indeed not at the redshift of the cluster.

2.4. KMOS Observations

Observations were prepared with the KMOS Arm Allocator (KARMA; Wegner & Muschielok 2008) allocating 19–20 arms to objects and 1–3 arms to faint stars, which were used to monitor both the PSF and the photometric conditions during the observations; when more than one star was allocated, we used arms corresponding to different KMOS detectors. The total number of galaxies in the *red sequence* of the CMDs within the limits described in Section 2.3.2 that were selected for KMOS observations of XMM2235, XMM2215, and Cl0332 is 56.

Observations of the cluster galaxies were obtained between 2013 October 30–November 16, 2014 July 6–19, 2014 October 19–21, 2015 September 17–19, 2015 October 10–12, and 2016 September 7–10 using the KMOS *YJ* band filter covering the wavelength interval 1–1.36 μm. Data for XMM2215, Cl0332, and the second mask of XMM2235 were taken with a standard object-sky-object nodding pattern in which each on-source frame has an adjacent sky exposure. For the first mask of XMM2235, we used a technique developed for very crowded regions, in which we alternated IFUs on sky and objects, allowing us to collect 100% of the time on-source, but in half of the objects compared to the two other clusters. With two of these allocations, we obtain the same number of objects we observed in the other two clusters. Our single-exposure times range from 300 s for XMM2215, Cl0332 and the second mask of XMM2235 to 450 s for the first mask of XMM2235. Each exposure was dithered by 0.1 $-0\farcs6$ to improve bad-pixel rejection from the final extracted spectra. The median integration time per target is ~18 hr on source for our first mask in XMM2235 and ~10 hr on source for the second mask, ~19 hr on source for objects from XMM2215, and ~16 hr on source for objects from Cl0332. We further apply additional quality cuts (i.e., seeing FWHM $< 1''$), such that the final exposure varies on a galaxy-by-galaxy basis. The actual exposure time for the first mask of XMM2235 ranges between 14 and 21 hr on source, between 5 and 16 hr on source in the second mask, between 18 and 20 hr for XMM2215, and between 6 and 17 hr for Cl0332.

Telluric stars of spectral type O or A0 were observed as standard calibrations.

2.5. KMOS Data Reduction

Data reduction was performed using a combination of the Software Package for Astronomical Reductions with KMOS pipeline tools (`SPARK`; Davies et al. 2013) and custom Python scripts (Mendel et al. 2015, J. T. Mendel et al. 2017, in preparation). `SPARK` tools were used for bad-pixel-mask creation, flat fielding, and wavelength calibration. Science frames were corrected for a channel-dependent bias drift using reference pixels on the perimeter of each detector before reconstructing the data cubes. The illumination correction was performed using the observed sky-line fluxes on a frame-by-frame basis. Sky subtraction was performed in two steps. We first performed a simple A-B subtraction, and then applied a second-order correction for the residuals by stacking the spectra per detector. This second-order correction effectively accounts for both the variability of OH lines flux and system flexure.

We performed a 1D optimal extraction (e.g., Horne 1986) for the targeted galaxies and used the *HST* images in a band close to our KMOS observations to describe how the galaxy flux is distributed within the IFU (see Mendel et al. 2015, J. T. Mendel et al. 2017, in preparation).

In summary, the center of the galaxy in each KMOS frame within an acquisition was aligned to the *HST* postage stamp position. The shifts were derived from the dither pattern applied in the observations and some additional centering accounting for the KMOS positioning inaccuracy ($\sim 0\farcs2$). *HST* images were convolved to match the PSF measured from reference stars in each exposure. We used the segmentation maps derived for the source catalogs to mask neighboring objects and help optimize the extraction. The spectra were extracted by combining the galaxy flux in the KMOS IFU within the half-light radius of the galaxy, following a weighting scheme and rejection criteria. As an intermediate step, a telluric correction using both telluric stars and model atmosphere through the code `MOLECFIT` (Kausch et al. 2014) was applied, as well as a flux calibration.

We constructed 100 bootstrap realizations of the final 1D spectrum by randomly selecting (with replacement) from the input frames; the realizations were used to estimate the uncertainties on the extracted spectra.

3. Galaxy Properties

3.1. Structural Parameters

Structural parameters are derived in Chan et al. (2016) and Chan et al. (2017). We use an adapted version of `GALAPAGOS` (Barden et al. 2012), which includes the 2D light profile modeling from `GALFIT v.3.0.5` (Peng et al. 2010). We perform 2D Sérsic (1968) fits, accounting simultaneously for neighboring objects and deriving the PSF from bright stars in the field. We construct catalogs of structural parameters including semimajor axis effective radii, $a_{\rm e}$, Sérsic index n, and magnitude in different ACS and WFC3 bands (see Chan et al. 2016 and Chan et al. 2017). For each overdensity we select parameters derived in the observed band closer to the rest-frame *B* band of the local Coma FP (e.g., Jørgensen et al. 2006). For XMM2215, there is no available band exactly corresponding to the rest-frame *B* band, therefore we resort to using the ACS $z_{\rm F850lp}$ effective radii and apply a wavelength-dependent correction to the bluer effective radii, following the prescriptions described in Section 5.1 of Chan et al. (2016).

For XMM2235, simulations show that our method produces measurements of the semimajor axis $a_{\rm e}$ with a systematic bias of -0.4% and a 1σ dispersion lower than 31% for objects with $Y_{\rm F105w}$ surface brightness brighter than 22.75 mag arcsec^{-2}. Similarly, for XMM2215, we recover $a_{\rm e}$ with a systematic bias of 1% and a 1σ dispersion lower than 49% for objects with $z_{\rm 850lp}$ surface brightness brighter than 23.25 mag arcsec^{-2}. For Cl0332, we recover $a_{\rm e}$ with a systematic bias of 1% and a 1σ dispersion lower than 5% for objects with $J_{\rm 125w}$ surface brightness brighter than 20.75 mag arcsec^{-2} (see Chan et al. 2016 and Chan et al. 2017).

Effective radii are circularized following $R_{\rm e} = \sqrt{ab}$, where a and b are the semimajor and minor axis, respectively. For our sample, the median errors on $R_{\rm e}$ range from 0.79, 1.01, to 0.22 kpc, corresponding to 31%, 37%, and 11% for XMM2235, XMM2215, and Cl0332, respectively.

Appendix A of Chan et al. (2017) shows that our structural parameters for the galaxies in Cl0332 are consistent with publicly available measurements by van der Wel et al. (2014) in the GOODS-S deep field (median difference of -0.029 dex, and 1σ dispersion of 0.046 in $\log R_{\rm e}$).

We derive absolute magnitudes in the rest-frame B band Johnson following Equation (2) of Hogg et al. (2002), which includes the apparent magnitude of our galaxies in the observed band, the distance modulus at the redshift of each galaxy, and the K-corrections from observed to rest-frame band (e.g., Oke & Sandage 1968; Hogg et al. 2002). The K-corrections account for the factor $(1 + z)$ related to the flux change with redshift.

Given the limited amount of available photometric bands for our sample, we resorted to calculating K-corrections for Maraston (2005) simple stellar population models (SSPs) with solar metallicity and spanning the color range of our red-sequence galaxies. Following Equation (2) of Hogg et al. (2002), the K-correction from one observed band to the rest-frame B band can be obtained when we know the absolute magnitudes in B band of the SSPs, their apparent magnitude in the observed band, and the distance modulus as a function of redshift and SSP observed band. We obtain the above-mentioned quantities for Maraston (2005) SSPs using the code `EzGal` of Mancone & Gonzalez (2012). We fit quadratic functions between the model K-corrections and their colors and derive the appropriate K-correction for our galaxies; the scatter of the relation was added in quadrature to the uncertainties of the magnitudes. Median values of the K-correction from $Y_{\rm F105w}$ to B band for XMM2235 are -0.96 mag, from $z_{\rm 850lp}$ to B band 0.06 mag for XMM2215, and from $J_{\rm F125w}$ to B band -1.36 mag for Cl0332. We find similar K-corrections when we adopt Bruzual & Charlot (2003) SSPs with solar metallicity.

We derive the mean surface brightness within $R_{\rm e}$, $\langle I_{\rm e}\rangle$ by dividing the total luminosity in the rest-frame B band by $2\pi R_{\rm e}^2$ (with $R_{\rm e}$ in pc), assuming a B-band solar magnitude in AB of $M_{\odot,B} = 5.36$ from Table 1 of Blanton & Roweis (2007).

All the parameters for the galaxies that are part of our dispersion sample are summarized in Table 1.

3.2. Stellar Masses

We use the stellar masses $M_\star$ from Chan et al. (2016) and Chan et al. (2017). These masses are derived using an empirical $M_\star/L$–color relation (e.g., Bell & de Jong 2001; Bell et al. 2003) calibrated on the multiband photometric catalogs of the NEWFIRM Medium-band Survey (NMBS; Whitaker et al. 2011) based on Bruzual & Charlot (2003) templates, an exponentially declining star formation history and a Chabrier (Chabrier 2003) initial mass function (IMF). We correct from aperture to total $M_\star$ using the best-fit Sérsic luminosity. Typical uncertainties range from ∼0.05 to 0.13 dex and include photometric uncertainties in color and luminosity as well as the scatter in the derived $M_\star/L$–color relation, but do not include systematics like different IMFs. Stellar masses for the dispersion sample are listed in Table 1. The stellar masses we use are consistent with catalogs available in the literature (see Chan et al. 2016 and Chan et al. 2017). For XMM2235, we find a median difference $\Delta \log M_\star = \log M_{\star,\rm literature}$–$\log M_{\star,\rm our} = 0.03$ dex and 1σ scatter of 0.09 dex with respect to $\log M_\star$ measurements by Delaye et al. (2014), and for XMM2215, we find $\Delta \log M_\star = -0.08$ dex and 1σ scatter of 0.14 dex from the $M_\star$ measure in the same paper. For Cl0332, we find $\Delta \log M_\star = -0.05$ and 1σ scatter of 0.08 dex compared to $M_\star$ derived by Momcheva et al. (2016), and $\Delta \log M_\star = -0.05$ and 1σ scatter of 0.06 dex compared to $M_\star$ derived by Santini et al. (2015).

3.3. Stellar Velocity Dispersions

We measure stellar velocity dispersions σ with the Penalized PiXel-Fitting method (`pPXF`) of Cappellari & Emsellem (2004); Cappellari (2017), using as templates the Maraston & Strömbäck (2011) SSPs based on the ELODIE v3.1 stellar library (Prugniel & Soubiran 2001; Prugniel et al. 2007). The ELODIE-based templates cover the wavelength range between 3900 and 6800 Å, which matches the rest-frame wavelength of our KMOS data, and have higher resolution (FWHM of 0.55 Å) than the median rest-frame KMOS FWHM (∼1.5 Å). We did not use the more commonly used Maraston & Strömbäck (2011) SSPs based on the MILES library (Sánchez-Blázquez et al. 2006 with resolution 2.54 Å as derived in Beifiori et al. 2011) to allow us to derive stellar velocity dispersion in less massive objects as well. We tested that our results are independent of the template library we used.

The KMOS spectra have a wavelength-dependent line-spread function as measured from the sky lines. Therefore they are smoothed with a variable kernel to match the maximum FWHM in each IFU before fitting the kinematics. Whether we use this smoothing or not does not change our measurements. Consistently, Maraston & Strömbäck (2011) ELODIE-based templates are broadened to match the new KMOS resolution. Before the `pPXF` fit, the KMOS spectra are cross correlated with a 1 Gyr old Maraston & Strömbäck (2011) template to obtain an initial estimate for the redshift of the galaxy.

We use additive polynomials of low order, generally 2–3, to account for uncertainties in the sky subtraction, which is one of the dominant factors of systematics in our data reduction, as well as any residual template mismatch. We test that the fit does not change by using polynomials of different orders (2–5): the large-scale variations included by the additive polynomial have a minimum impact on the scales of our line widths. The use of multiplicative polynomials of low order, together with or instead of additive polynomials, gives results consistent within the errors. During the fit, we also exclude regions with strong telluric and OH line features.

Stellar velocity dispersions are measured using the typical rest-frame optical features, such as Ca *H*&*K*, *G*-band, Balmer lines, and Mg (Bender 1990; Bender et al. 1994), depending on the cluster redshift; see e.g., Figure 3 for some examples of typical absorption lines. We measure the σ for 19 objects that constitute the dispersion sample; our fits are shown in Figure 3, and the derived parameters are summarized in Table 1. From our original sample, we mostly retained objects with measured stellar velocity dispersion at the cluster redshift, with $S/N > 5$, values of $\sigma_{\rm e} < 500\ {\rm km\ s^{-1}}$, and where the absorption-line features were clearly visible after a visual inspection of the fit.

We estimate uncertainties on σ using the 100 bootstrap realizations of the extracted spectra and recomputing the stellar velocity dispersion for each one of those. The errors on $\sigma_{\rm e}$ are the standard deviation of the distribution of the measurements

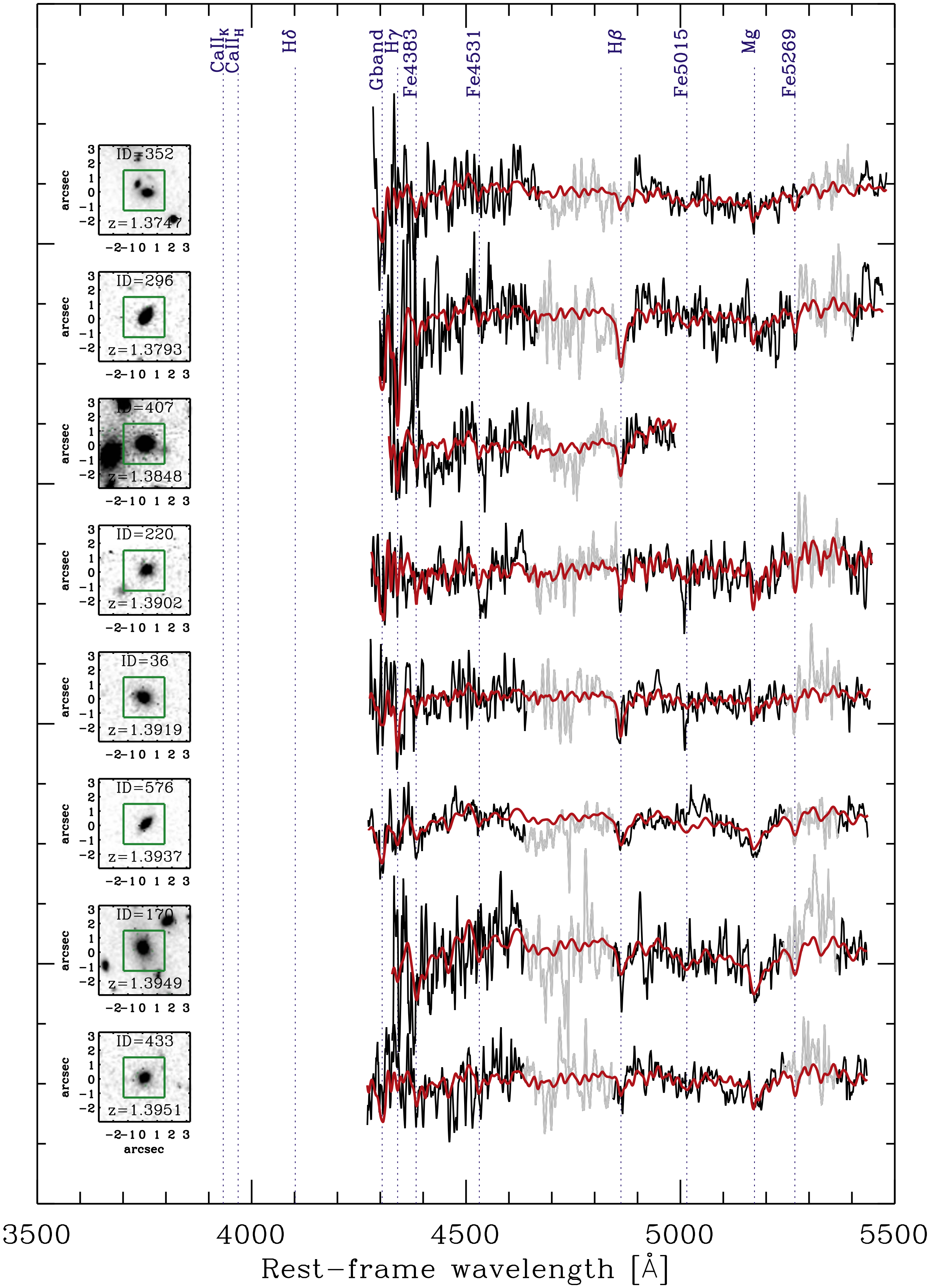

Figure 3. In black we show continuum-normalized inverse-variance-smoothed galaxy spectra with a window of seven pixels, ordered by redshift and shifted to rest-frame wavelengths. Kinematics fits are shown in red. In gray are plotted the regions with strong telluric features or OH residuals that were excluded from the fit. The most prominent spectral features are labeled at the top of the figure and are indicated by the dotted vertical lines. For each object we indicate IDs and redshifts from Table 1 and show the *HST* postage stamps (either WFC3/J_{F125w} or ACS/z_{F850lp}) of each galaxy of 6″ side; the KMOS IFU is drawn in green.

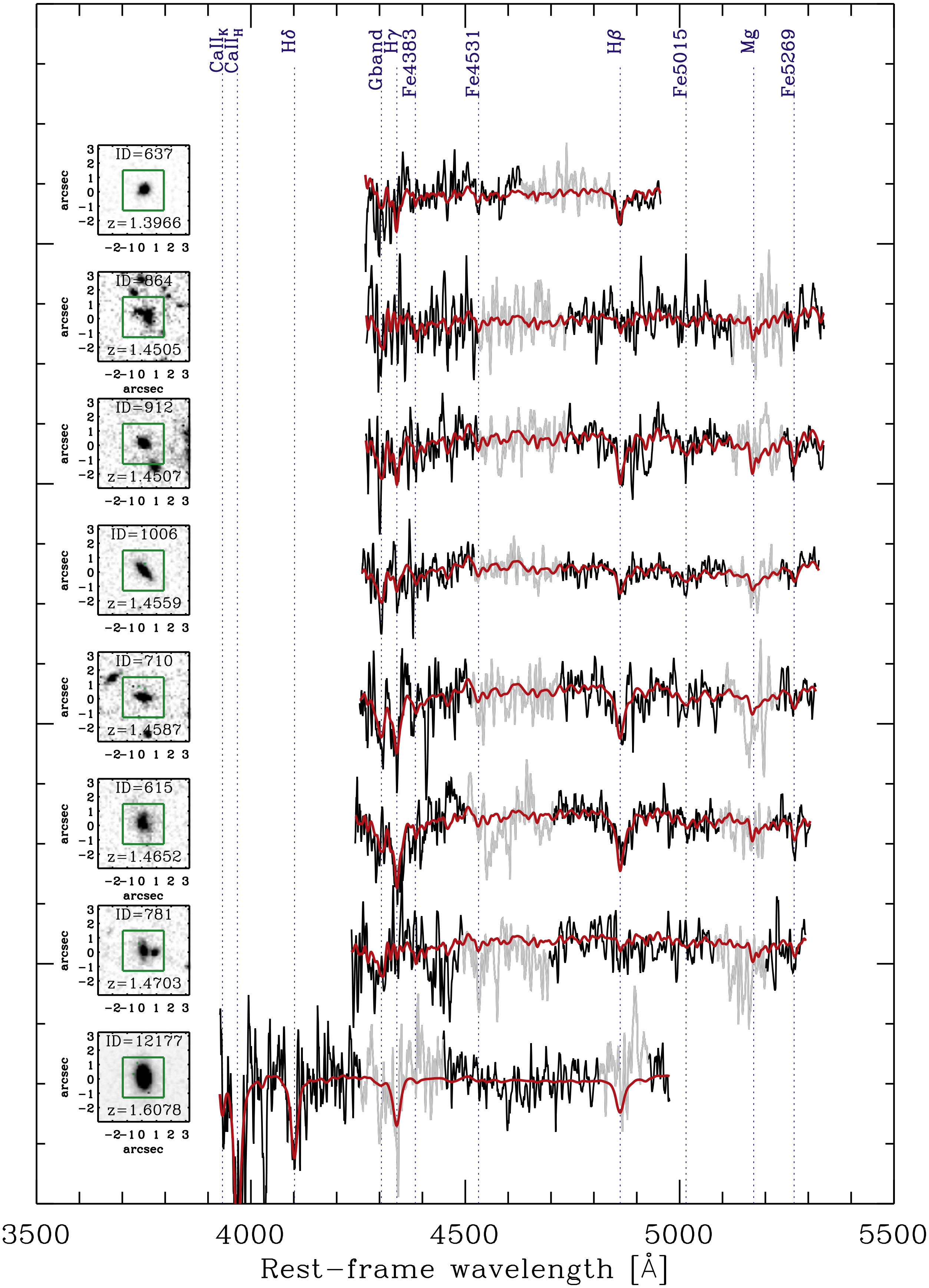

Figure 3. (Continued.)

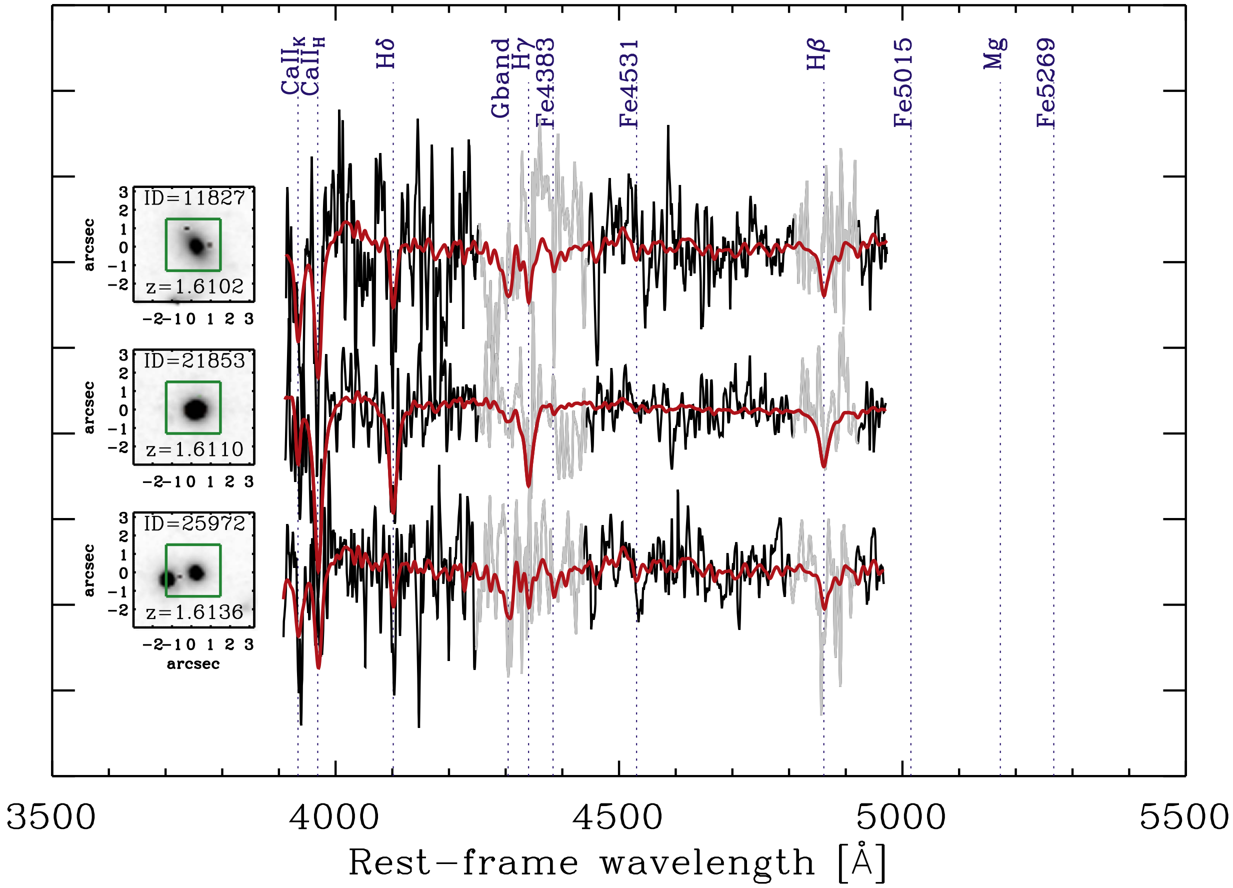

Figure 3. (Continued.)

of the bootstrap realizations. Typical errors are on the order of ∼11%–40% for galaxies with a typical S/N ∼ 5–12 per angstrom.

We perform tests to explore the robustness of our measurements by analyzing different wavelength ranges of the spectrum. This provides an assessment of the systematic effects arising from the derivation of stellar velocity dispersions from different absorption lines at different redshift. We repeated the fitting by considering only the "blue" and the "red" regions of our spectra and their bootstrap realizations (see Appendix A for details). For the two overdensities XMM2235 and XMM2215 where this test could be performed, the systematic offsets $\Delta \log \sigma_e$ between the full spectrum fit and the two subregions are usually <10%, and smaller than typical uncertainties on σ_e.

The KMOS 1D spectra are extracted within one R_e. Because the data are background dominated, the optimal extraction effectively makes our stellar velocity dispersions luminosity weighted within R_e, similarly to the measurements provided in the local universe. For this reason, no aperture correction is needed, and we therefore use the notation σ_e for σ throughout the paper.

3.3.1. Dynamical Masses

Dynamical masses $M_{\rm dyn}$ are derived following the prescriptions of Cappellari et al. (2006) by combining size and stellar velocity dispersion measurements as $M_{\rm dyn} = \beta(n) R_e \sigma_e^2 / G$, and assuming a Sérsic-index-dependent virial factor $\beta(n)$ (see Beifiori et al. 2014 for a similar approach). Typical uncertainties range from ∼0.10 to 0.40 dex. The effect of the change in dark matter fraction cannot be accounted for in this simple mass estimator. Moreover, another source for uncertainties is the unresolved rotation, which is not accounted for by our method. In fact, several works have shown that at both intermediate and high redshift, rotational support has an increasingly large contribution (van der Marel & van Dokkum 2007 at $z \sim 0.5$, and Newman et al. 2015; Hill et al. 2016; Belli et al. 2017; J. T. Mendel et al. 2017, in preparation, at $z > 1.4$). Our sample, in particular, XMM2235 and XMM2215, includes mostly objects with Sérsic index >2.5 where the impact of rotation is expected to be small based on the findings of Belli et al. (2017). Their Figure 7 shows that there is no trend in the ratio between stellar-to-dynamical mass as a function of the axis ratio, whereas for disk galaxies with Sérsic index <2.5, there is a clear trend matching the expectations for an increasing V/σ at high redshift. For Cl0332, half of the objects could potentially be affected because they have in general a lower Sérsic index than XMM2235 and XMM2215 (see Figure 4).

3.4. Distribution of Galaxy Properties and Selection Effects

Our sample does not appear to be systematically biased toward bluer galaxies, as found in previous kinematics samples at $z > 1.4$ (e.g., van de Sande et al. 2014) for XMM2235 and Cl0332; however, some bias could be present for XMM2215 (see Figure 2).

The empty histograms in Figure 4 show the distribution of circularized effective radii, effective surface brightness, a combination of size and surface brightness, Sérsic indices,

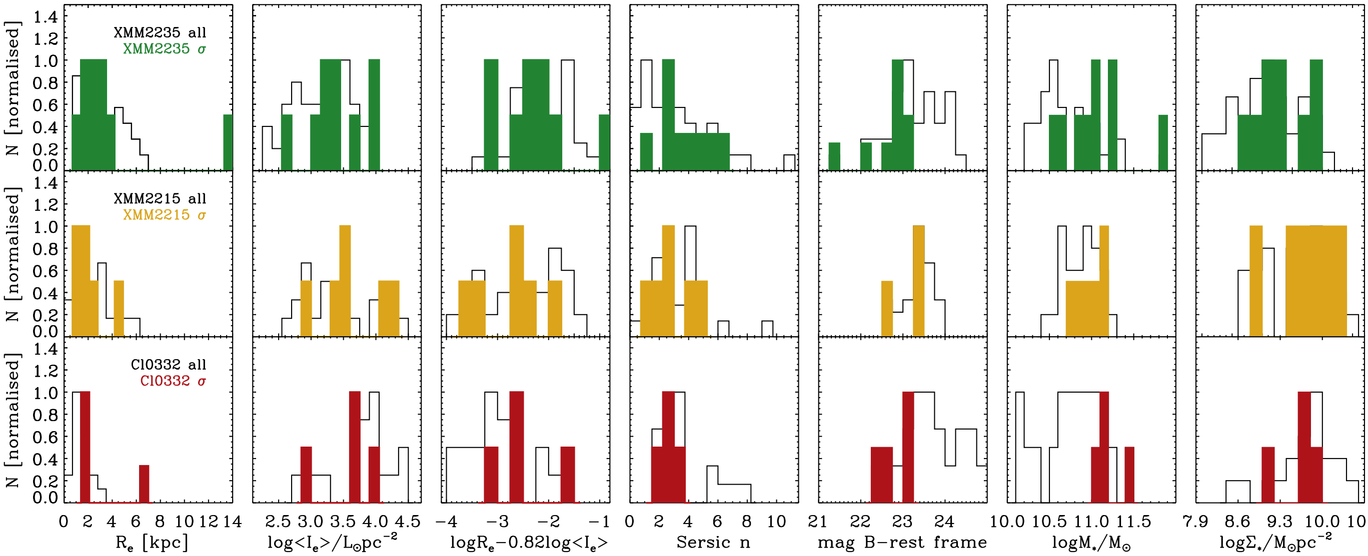

Figure 4. Normalized distribution of galaxy properties for the full red-sequence sample (black) and for the sample for which we measured σ_e (filled histograms). From top to bottom we see XMM2235, XMM2215, and Cl0332, in green, orange, and red, respectively. From left to right: circularized effective radii, surface brightness, combination of size and surface brightness, Sérsic index, B-band magnitude, stellar mass, and surface mass density. The sample with σ_e spans a similar range of galaxy properties as the underlying population on the red sequence, although the limited statistics makes the sample incomplete mostly at faint magnitudes and low stellar masses.

magnitudes, stellar masses, and surface mass density of the red-sequence objects of the three clusters, while the filled histograms show the distribution of our dispersion sample. Surface brightness and radii have similar distributions as the full sample, in particular for XMM2235. However, we mostly have successful σ_e measurements in the brightest and more massive galaxies.

A Kolmogorov–Smirnov test shows that the probability that the dispersion sample and the full red-sequence sample are drawn from the same parent distributions in magnitude and stellar mass is ∼1 and 13% for XMM2235, ∼24 and 55% for XMM2215, and 1 and 3% for Cl0332. We are mostly unable to measure the stellar velocity dispersion in faint objects.

We also perform a k-sample Anderson–Darling test (Scholz & Stephens 1987) on the same parameters of Figure 4 to assess whether the tail of the cumulative distributions can affect our results. We find that the null hypothesis that the dispersion sample and the full red-sequence samples are drawn from the same distribution in magnitude and stellar mass can be rejected at 1% and 5% for XMM2235, ∼20% for XMM2215, and 2% and 5% for Cl0332. For other parameters such as R_e, $\log\langle I_e\rangle/(L_\odot\ \mathrm{pc}^{-2})$, and the Sérsic index, the null hypothesis cannot be rejected for XMM2235 and XMM2215.[10] For Cl0332, the distribution of R_e is not compatible with the null hypothesis with a p-value of 20%.

We therefore conclude that our observations are not representative of the whole red-sequence sample in terms of stellar mass, or magnitude for the three overdensities in our sample: for this reason, in Section 5.2 we make a cut to a common stellar mass limit.

We assess the selection effects and the success rate for the three clusters by deriving selection probabilities P_s for each galaxy with a method similar to that used by Saglia et al. (2010a) (see Appendix B for details). In summary, P_s are calculated accounting for the completeness in the measured stellar velocity dispersion, rescaled by the ratio of spectroscopically confirmed members over the targets we observed with KMOS. The inverse of each P_s is used as weight in the fits performed in Section 5.2 to assess whether the use of our dispersion sample could bias our results.

4. Local and Intermediate-redshift Comparison Samples

4.1. The Coma Cluster

As a local comparison sample, we use the Coma cluster with a mass $M_{200} = (1.6 \pm 0.4) \times 10^{15}\ h^{-1}\ M_\odot$ (rescaled mass from Łokas & Mamon 2003, see also Figure 1 and Section 2.2), which is usually adopted as a reference cluster for FP and scaling relations studies (see e.g., Jørgensen et al. 2006; Thomas et al. 2007; Cappellari 2013; Houghton et al. 2013).

The photometry used to derive the local FP relation by Jørgensen et al. (2006) is not public, therefore we adopt the structural parameters and magnitudes from Table A2 of Holden et al. (2010). The photometric parameters come from the surface brightness analysis to the SDSS g-band images by Holden et al. (2007), who transformed them from SDSS bands to the rest-frame B band. The photometry of Holden et al. (2007) is consistent with the photometry used in the initial work on the Coma FP by Jørgensen et al. (1996) (see description in Section 2.2.1 of Holden et al. 2007 and Appendix A2 of Holden et al. 2010) for the objects in common, but expanded to a larger number of objects with stellar velocity dispersion from Jørgensen et al. (1995) and Jørgensen (1999) (which in total are 116 galaxies), making up a sample of 80 galaxies with both stellar velocity dispersion and structural parameters. In Holden et al. (2010), effective radii are given in the g band; we assume them to be comparable to rest-frame B band radii throughout the paper.

Dynamical masses are computed from the σ_e, R_e, and Sérsic n given in Table A2 of Holden et al. (2010), using the approach of Section 3.3.1, as for our KCS sample. The Coma cluster was targeted by the SDSS photometry, therefore we use stellar masses from the SDSS catalog of Maraston et al. (2013). Maraston et al. (2013) stellar masses were derived from the

---

[10] We note that for XMM2215, the null hypothesis cannot be rejected also considering the distribution of $M_\star$.

spectral energy density (SED) fitting of the five SDSS bands and were based on Maraston et al. (2009) stellar population models and a Kroupa (2001) IMF. We homogenize $M_\star$ to a common Chabrier IMF and account for the difference in the stellar population models used by adopting the offsets provided in Table B3 of Pforr et al. (2012),[11] which were derived for mock passive galaxies for different population models (see detailed description of the method in Beifiori et al. 2014). We test that similar results are obtained when we use other $M_\star$ catalogs of SDSS galaxies (e.g., Mendel et al. 2014). The rescaling of the stellar masses to the best-fit Sérsic luminosity has a minimum effect on the mass estimate we use. The Coma sample is our local reference throughout the paper, therefore we do not apply the mass cut we have in our KMOS sample at $\log M_\star/M_\odot > 10.5$ to minimize the bias on the scaling relations we derive.

We compare our Coma catalog with the catalog of Cappellari (2013), which includes effective radii in K band and dynamical masses for a K-band selected sample of 161 galaxies within a magnitude limit of $M_K < -21.5$. This sample includes both early-type galaxies and spirals (∼10%). There are 90 objects in common between the two samples, 66 of which have measured sizes from Holden et al. (2010). We find consistent distributions of sizes and masses between the two samples. For the objects in common, we find that sizes are mostly consistent ($\Delta \log R_{\rm e} = \log R_{\rm e,Holden} - \log R_{\rm e,Cappellari} \sim -0.03$ dex and scatter 0.16 dex), while stellar and dynamical masses are offset in respect to the masses of Cappellari (2013) ($\Delta \log M = \log M_{\rm Cappellari} - \log M_{\rm our}$) of ∼0.14 dex and ∼−0.16 dex, respectively, where we included a factor ∼0.08 dex in our measured stellar masses because of the different aperture used in deriving stellar and dynamical masses (see Appendix A of Beifiori et al. 2014). These differences do not affect our conclusion.

The full Coma sample includes galaxies with a range of properties: some of them may not descend from our high-redshift galaxies (e.g., "progenitor bias" van Dokkum & Franx 2001; Saglia et al. 2010a; Valentinuzzi et al. 2010; Carollo et al. 2013; Poggianti et al. 2013; Beifiori et al. 2014). Several studies have found a relation between the size and the age of passive galaxies at intermediate and high redshift (e.g., Valentinuzzi et al. 2010; Poggianti et al. 2013; Belli et al. 2015; Shetty & Cappellari 2015, but see also Fagioli et al. 2016 for different opinions), suggesting that the selection of old galaxies could minimize the descendant/progenitor mismatch. Following this idea, we select Coma galaxies whose ages are older than the difference between the look-back times of Coma and our highest redshift KCS overdensity (e.g., >9 Gyr), following a procedure similar to that of Beifiori et al. (2014); Chan et al. (2016). Ages for Coma galaxies are derived from the line indices measurements of Jørgensen (1999) (their Table 4 contains measurements for 70 galaxies) using Maraston (2005) stellar population models, and following the method described by Saglia et al. (2010b). The resulting sample with an age >9 Gyr consists of six galaxies.

4.2. The EDisCS-cluster Sample

The intermediate-redshift comparison sample comes from the cluster galaxies at median redshift $z \sim 0.7$ used for the FP work of the EDisCS survey (Saglia et al. 2010a, see also Figure 1 and Section 2.2). The full EDisCS-cluster sample includes 26 clusters or groups with redshift between $0.4 < z < 0.9$ and a velocity dispersion between 166 and 1080 km s^{-1} (Milvang-Jensen et al. 2008; Saglia et al. 2010a). In this paper we consider a subsample of 10 clusters out of the 14 with available *HST* photometry, for which both Sérsic fits and stellar masses were derived (see Figure 1). Catalogs include structural parameters from Simard et al. (2009), stellar velocity dispersions from Saglia et al. (2010a), and updated $M_\star$ from G. Rudnick et al. (2017, in preparation) derived using the `iSEDfit` software (Moustakas et al. 2013), Bruzual & Charlot (2003) models and a Charbier IMF; stellar masses were also rescaled for the missing flux using the best-fit Sérsic luminosity similarly to our KCS sample. Dynamical masses are derived as in Section 3.3.1. We select galaxies with $\log M_\star/M_\odot > 10.5$, to be consistent with the stellar mass limit of our KMOS sample. For some of the tests in Section 5.2, we applied an additional mass cut $\log M_\star/M_\odot > 11$ to match the mass limit of our highest redshift overdensity. In this case, we also select a subsample of galaxies with an age >3 Gyr to minimize progenitor bias. Ages for EDisCS galaxies were collected from Sánchez-Blázquez et al. (2009). The resulting sample consists of 56 galaxies, which we identify as the EDisCS-cluster sample ("EDisCS-cl") throughout the paper.

5. Results

5.1. The FP of KCS Galaxies

We consider the edge-on projection of the FP as

$$\log R_{\rm e} = a \log \sigma_{\rm e} + b \log \langle I_{\rm e} \rangle + c_z, \tag{1}$$

where $R_{\rm e}$ is measured in kpc, $\sigma_{\rm e}$ in km s^{-1}, $\log\langle I_{\rm e}\rangle$ is in $L_\odot$ pc^{-2}, c_z is the redshift-dependent zero-point of the relation, and $a = 1.30 \pm 0.08$ and $b = -0.82 \pm 0.03$ come from the local B-band FP of Jørgensen et al. (2006).

Owing to the limited number of objects in our sample, we assume that the local slopes are still valid at high redshift. We note that some variations of the coefficients were reported by previous work at $z \sim 1$ (e.g., Treu et al. 2005; van der Wel et al. 2005; di Serego Alighieri et al. 2005; Renzini 2006; Saglia et al. 2010a; Jørgensen & Chiboucas 2013).

We determine the zero-point of our KCS galaxies by performing a least-squares fit using the `MPFITEXY` routine (Williams et al. 2010), by accounting for the errors in both coordinates, no intrinsic scatter, and assuming that the slopes are fixed to the local value. The `MPFITEXY` routine depends on the `MPFIT` package (Markwardt 2009). Errors are obtained with a jackknife method.

The left panel of Figure 5 shows the edge-on projection of the FP for our KCS sample compared to the EDisCS sample (Saglia et al. 2010a) and the Coma relation of Jørgensen et al. (2006). The zero-point evolves with redshift from the value 0.443 of Coma in B band (Jørgensen et al. 2006, at $z = 0.023$) to 0.22 ± 0.02 at the median $z \sim 0.7$ of EDisCS-cl to -0.10 ± 0.09, -0.19 ± 0.05, and -0.29 ± 0.12 for XMM2235 at $z = 1.39$, XMM2215 at $z = 1.46$, and Cl0332 at $z = 1.61$, respectively. We note that the zero-points are derived including the full sample of galaxies from the three KCS clusters. The rms scatter of the relations ranges from 0.08 for Coma to $\sim 0.15 \pm 0.05$ for EDisCS-cl, to $\sim 0.09 \pm 0.02$

---

[11] We note that the offset provided in Table B3 of Pforr et al. (2012) is for galaxies at $z = 0.5$. At the redshift of Coma, this represents an upper limit on the offset we need to apply.

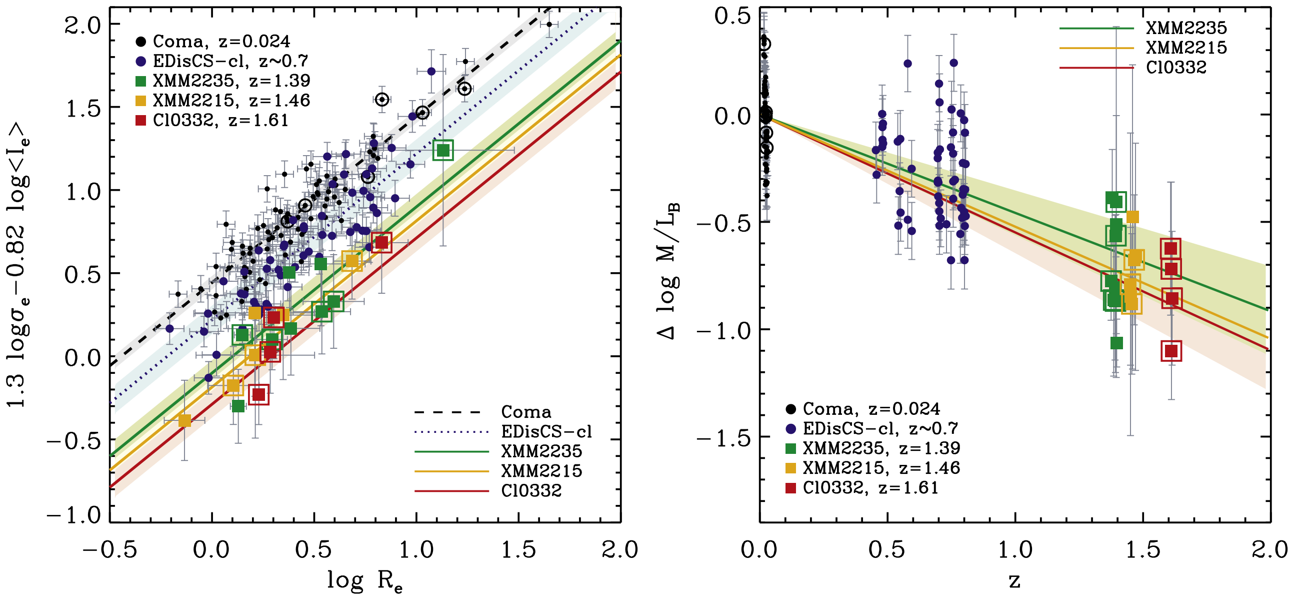

Figure 5. Left panel: edge-on projection of the FP. The Coma FP of Jørgensen et al. (2006; black dashed line and black filled circles) and the FP from EDisCS clusters at $z \sim 0.7$ of Saglia et al. (2010a; blue dotted line and blue filled circles) are included as reference. Open black circles show only Coma galaxies with an age >9 Gyr. KCS galaxies (green, orange, and red filled squares) follow the FP scaling relation, but are offset (green, orange, and red solid lines) with respect to Coma and EDisCS. Open squares for our KCS sample show galaxies for which $\log M_\star/M_\odot > 11$. Shaded regions show the 1σ scatter. Right panel: redshift evolution of $\Delta \log M/L_B$. Each solid line (green, orange, and red) shows the best-fit linear relation for Coma and the galaxies in each of the KCS overdensities with $\log M_\star/M_\odot > 11$ (excluding EDisCS from the fit, see the text). Shaded regions show the 1σ errors on the slope. The shaded region for XMM2215 is covered behind that of XMM2235 and Cl0332.

for XMM2235, ∼0.09 ± 0.02 for XMM2215, and to ∼0.16 ± 0.07 for Cl0332.

We test that the photometry we use for the Coma galaxies allows us to recover the zero-point of Coma by Jørgensen et al. (2006) within the errors of about ∼0.02. We also test whether the use of Coma galaxies with older ages affects our results. We fix the coefficients a and b of the FP of Jørgensen et al. (2006) and derive the zero-point c_z using subsamples selected with increasingly larger age limit, up to our progenitor bias limit of >9 Gyr. Our test shows that the zero-point varies at most by 0.02, suggesting that the use of the full Coma sample does not bias our results; for this reason, we can assume the same zero-point as was derived by Jørgensen et al. (2006) throughout the paper.

5.2. The M/L Evolution with z

Under the assumption of homology (i.e., that the coefficients a and b are constant with redshift, see Section 5.1), the zero-point of the FP traces the mean galaxy $\Delta \log M/L$. Therefore, we can convert the zero-point change into an evolution of the $\Delta \log M/L$ ratio with redshift such that

$$\Delta \log(M/L)_z = \log(M/L)_z - \log(M/L)_{\rm Coma} = (c_z - c_{\rm Coma})/b, \qquad (2)$$

where $c_z = \log R_{\rm e} - (a \log \sigma_{\rm e} + b \log\langle I_{\rm e}\rangle)$ based on Equation (1) and $c_{\rm Coma}$ is the Coma zero-point of Jørgensen et al. (2006). The error on the Coma zero-point is not provided by Jørgensen et al. (2006), therefore we obtained it from our Coma sample with a jackknife method as described in Section 5.1.

The right panel of Figure 5 shows the evolution of the $\Delta \log M/L$ as a function of redshift. The overdensities in our sample have different properties and masses (see Section 2.2), therefore we could expect different mean ages for our galaxies. For this reason, we separately fit our KCS galaxies, using Coma as a reference value. The use of the Coma cluster to define the zero-point is arbitrary because it is a normalization term, and it does not affect our analysis. Our intermediate-redshift EDisCS-cl sample has significantly smaller error bars than our KCS clusters. In Table 2 we show that this drives the fit toward the slopes preferred by the EDisCS-cl sample. For this reason, we resort to giving the slope-derived fitting only to Coma and KCS galaxies.

To make a fair comparison between different overdensities, we consider the $\Delta \log M/L$ evolution for a sample with the same mass distribution in the three overdensities. We apply a mass cut of $\log M_\star/M_\odot > 11$ to the sample of XMM2235 and XMM2215 to match the minimum $M_\star$ for the objects in Cl0332. This mass limit is also known to provide an unbiased measure of the M/L evolution, as discussed in van der Marel & van Dokkum (2007) and van Dokkum & van der Marel (2007). We obtain $\Delta \log M/L_B = (-0.46 \pm 0.10)z$, $\Delta \log M/L_B = (-0.52 \pm 0.07)z$, and $\Delta \log M/L_B = (-0.55 \pm 0.10)z$ for XMM2235, XMM2215, and Cl0332, respectively. Error bars were estimated with a jackknife method. In XMM2235 and XMM2215, we were able to derive stellar velocity dispersions also in galaxies with $10.5 < \log M_\star/M_\odot < 11$. When we include them in our analysis, we obtain slightly steeper $\Delta \log M/L_B = (-0.54 \pm 0.13)z$, although consistent within the errors, for XMM2235 and consistent $\Delta \log M/L_B = (-0.52 \pm 0.04)z$ for XMM2215.

The $\Delta \log M/L$ evolution for the massive galaxies of XMM2215 and Cl0332 is consistent with the results by Saglia et al. (2010a) and van Dokkum & van der Marel (2007), but slightly steeper than van Dokkum & Stanford (2003), Wuyts et al. (2004), and Holden et al. (2005). The $\Delta \log M/L$ evolution for the massive galaxies of XMM2235 is smaller. van de Sande et al. (2014) found similar small $\Delta \log M/L$ evolution from studying a sample of field galaxies at $z \sim 1.5$ and applying a correction for the fact that galaxies in their sample are bluer than a representative parent sample of quiescent galaxies from the 3DHST survey

Table 2
Evolution of $\Delta\log M/L_B$ with Redshift

Case	Relation	XMM2235	XMM2215	Cl0332
1	$\Delta\log M/L_B = \eta\log(1+z)$, KCS, $\log M_\star/M_\odot > 11$	-1.68 ± 0.37	-1.91 ± 0.25	-2.10 ± 0.37
2	$\Delta\log M/L_B = \eta\log(1+z)$, EDisCS-cl+KCS, $\log M_\star/M_\odot > 11$	-1.33 ± 0.13	-1.28 ± 0.15	-1.32 ± 0.15
3	$\Delta\log M/L_B = \eta\log(1+z)$, EDisCS-cl+KCS, $\log M_\star/M_\odot > 11$ & M_{200}	-1.44 ± 0.15	-1.18 ± 0.16	-1.32 ± 0.21
4	$\Delta\log M/L_B = \eta\log(1+z)$, all KCS	-1.98 ± 0.46	-1.92 ± 0.15	-2.10 ± 0.37
5	$\Delta\log M/L_B = \eta\log(1+z)$, KCS, $\log M_\star/M_\odot > 11$ & P_s	-1.65 ± 0.41	-1.93 ± 0.23	-2.17 ± 0.41[a]

Note. Evolution of $\Delta\log M/L_B$ for our five test cases: (1) KCS galaxies with $\log M_\star/M_\odot > 11$, (2) $\log M_\star/M_\odot > 11$ galaxies part of the EDisCS-cl and KCS, (3) $\log M_\star/M_\odot > 11$ galaxies part of the EDisCS-cl and KCS, but with EDisCS-cl sorted based on their M_{200} to match that of the three KCS overdensities, (4) the full sample of galaxies for which we derived the stellar velocity dispersion in KCS, and (5) the KCS galaxies with $\log M_\star/M_\odot > 11$ in which selection weights P_s are applied.

[a] -2.18 ± 0.37 is the slope we obtain when we apply the selection weights derived for the full GOODS-S structure.

(Brammer et al. 2012; Skelton et al. 2014). As shown in Figure 2, our sample does not appear to be biased toward blue objects in XMM2235 and Cl0332; for XMM2215, we note that the majority of the objects are in the bluer part of the red sequence.

We now express the evolution of $\log M/L$ as $\Delta\log M/L_B = \eta\log(1+z)$, where η is the slope of the logarithmic dependence. This parametrization allows us to compare the amount of $\Delta\log M/L$ evolution compared to the structural evolution with redshift in our sample (see Section 6.2).

We derive the evolution considering different combinations of the available data, which are summarized in Table 2. Case (1) shows the results for only KCS galaxies with $\log M_\star/M_\odot > 11$; case (2) $\log M_\star/M_\odot > 11$ galaxies part of the full sample of EDisCS-cl and KCS; case (3) includes $\log M_\star/M_\odot > 11$ galaxies part of the EDisCS-cl and KCS, but with EDisCS-cl sorted based on their M_{200} (see Figure 1) to match that of the three KCS overdensities[12]; in case (4) we include also KCS galaxies with $\log M_\star/M_\odot > 10.5$ in XMM2235, and XMM2215; and case (5) we use only KCS galaxies with $\log M_\star/M_\odot > 11$ for which we apply the selection weights P_s we describe in Section 3.4 and derive in Appendix B. Error bars are estimated with a jackknife method.

In case (1), we find that the slopes η are consistent within the errors for the three KCS overdensities, with a weak suggestion that the slope of XMM2235 is slightly flatter than that of Cl0332.

In cases (2) and (3), we generally find flatter slopes, which are consistent between the three KCS overdensities, and smaller error bars. We note that the actual value of the slopes in these two cases is fully driven by the EDisCS-cl data, which have significantly smaller error bars than our KCS clusters. To avoid being biased toward the intermediate-redshift sample slopes, we refrain from using the EDisCS-cl sample in the following analysis and include the galaxies in our plots only for visual comparison.

In case (4), the derived slope η for XMM2235 is steeper, but still consistent within the errors with case (1). This is the result of the inclusion of the low mass, low σ_e objects in the fit. Our findings support the results of Treu et al. (2005) and Renzini (2006), who found a change in $\Delta\log M/L_B$ with galaxy mass with steeper $\Delta\log M/L_B$ in lower mass objects as result of recent star formation.

In case (5), we assess the effect of the sample selection and fit the $\Delta\log M/L$ evolution by applying the selection weights P_s we derive in Appendix B to the same sample we used in case (1). This allows us to up-weight the objects whose selection weights are smaller by scaling down their errors on the fitting procedure. We find values of η consistent within the errors with the case with no weights, with a weak tendency, given our error bars, to have flatter slopes for XMM2235 than for Cl0332, which instead become steeper. For Cl0332, the use of selection weights P_s calculated within the KMOS FoV and within the all GOODS-S structure give consistent results. We note that with this technique, we can only account for selection effects for the sample that we targeted at the cluster redshift.

6. Discussion

6.1. Formation Ages from the M/L Ratio Evolution

Passive evolution models are described by a formation redshift corresponding to the epoch of the last major star formation episode, which allows us to translate the $\log M/L$ and luminosity evolution into a formation age.

In order to derive formation ages from the $\log M/L$ ratio of our KCS galaxies, we use the tabulated M/L of the SSP models of Maraston (2005) with a Salpeter (1955) IMF and solar metallicity. We interpolate the models with a cubic spline to obtain an equally spaced $\log M/L$ grid in log *age*. We use solar metallicity Maraston (2005) SSPs, which is supported by both spectroscopic and photometry results of passive galaxies at high redshift (e.g., Mendel et al. 2015; Chan et al. 2016). In Appendix C we show the effect of using different SSPs and metallicity assumptions.

We test that our $\log M/L$ are consistent with the the $\log M/L$ we derive by fitting a linear relation between the logarithms of the age, metallicity, and M/L of Maraston (2005) SSPs with an age $\geqslant$1 Gyr and metallicity $\log Z/Z_\odot$ between -0.3 and 0.3 (total metallicity relative to solar), as done in Jørgensen et al. (2005), Jørgensen & Chiboucas (2013), and Jørgensen et al. (2014). In the following, we adopt the $\log M/L$ obtained via interpolation of the SSPs because the relation between M/L and log *age* becomes strongly nonlinear at young ages, which could potentially make our linear relation more uncertain.

Figure 6 shows Maraston (2005) SSPs for a range of formation redshifts $z_f = 1.8$–6 (dotted lines).

In our analysis we use relative M/L; therefore changes in the normalization of the IMF (i.e., changes in the low-mass slope) do not affect our conclusions. We note that nonstandard IMF

---

[12] We split EDisCS-cl into three samples: $M_{200} > 10^{15}\,h^{-1}\,M_\odot$ for XMM2235, $M_{200} > 10^{14}\,h^{-1}\,M_\odot$ for XMM2215, and $10^{13}\,h^{-1}\,M_\odot < M_{200} < 10^{14}\,h^{-1}\,M_\odot$ for Cl0332.

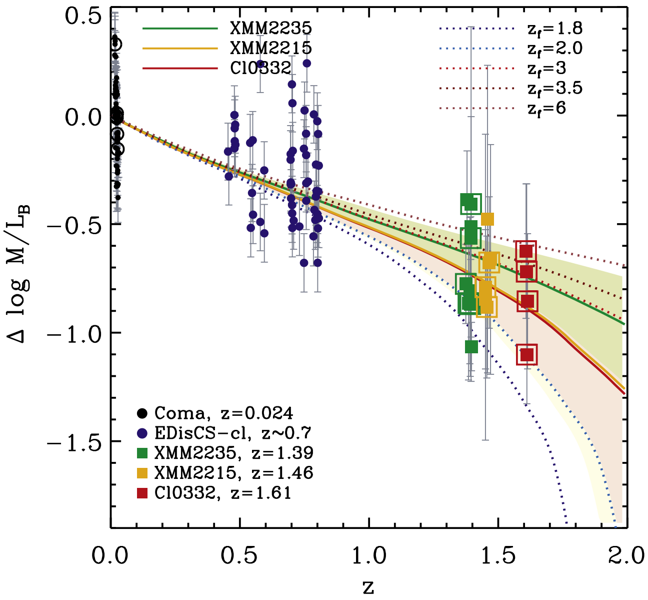

Figure 6. Redshift evolution of the $\Delta \log M/L_B$. Symbols are the same as in Figure 5. Dotted lines correspond to the predictions by Maraston (2005) SSPs for a Salpeter IMF, solar metallicity, and different formation redshifts. Each solid line (green, orange, and red) shows the SSP with a formation age corresponding to the age we derived for each cluster. Shaded regions show the 1σ error on the slope. The shaded region for XMM2215 is hidden behind that of XMM2235 and Cl0332.

slopes (i.e., non-Salpeter) would lead to different conclusion because of the known degeneracy between IMF and formation redshift (e.g., van Dokkum et al. 1998; Renzini 2006; van Dokkum & van der Marel 2007). The influence of the choice of the IMF will be discussed in a forthcoming paper.

We estimate the best-fit value and the 68% confidence interval of the formation ages by integrating the posterior likelihood distribution of the only free parameter, i.e., the formation age (or the formation redshift), given our data. We assume a top-hat prior on the formation redshift $z_f = 1.8$–6. We sampled the likelihood on a grid of formation redshifts within the prior.

The most massive galaxies in XMM2235 have a mean luminosity-weighted age of $2.33^{+0.86}_{-0.51}$ Gyr (formation redshift $z_f = 2.95^{+1.63}_{-0.54}$), while the mean age of XMM2215 is $1.59^{+1.40}_{-0.62}$ Gyr (formation redshift $z_f = 2.38^{+2.14}_{-0.44}$), and it is $1.20^{+1.03}_{-0.47}$ Gyr (formation redshift $z_f = 2.35^{+1.25}_{-0.34}$) for Cl0332. The ages of the three overdensities are consistent within the errors after accounting for the ~0.5 Gyr difference in the age of the universe between $z = 1.61$ and $z = 1.39$. There is a hint, albeit at low significance, that the ages of galaxies in Cl0332 are younger than the ages of XMM2235 galaxies. This weak suggestion is supported by our results from stacked spectra of the same galaxies, which will be described in R. C. W. Houghton et al. 2017, in preparation.

Cl0332 is by far the lowest density environment in our survey and shows ages on the order of field galaxies at similar redshift. When we compare the ages measured from stacked spectra of massive galaxies at the median redshift of $z = 1.75$ in the KMOS VIRIAL survey (e.g., Mendel et al. 2015, age of $1.03^{+0.13}_{-0.08}$ Gyr), we find that the two measures agree within the errors, after accounting for the 0.29 Gyr difference between the age of the universe at $z = 1.61$ and that at the median redshift of VIRIAL (see also Section 6.3).

We have verified that our results are consistent within the errors with ages obtained from the color evolution of SSPs compared to our galaxies.

By including in the sample of XMM2235 objects with $10.5 < \log M_\star/M_\odot < 11$, we derive slightly younger ages $\sim 1.63^{+0.39}_{-0.29}$ Gyr, suggesting a trend of age with $M_\star$, as discussed in Section 5.2, such that lower mass galaxies have younger ages than more massive objects. For XMM2215, we obtain consistent ages $\sim 1.62^{+1.30}_{-0.61}$ Gyr, which is probably due to the number of bluer objects that entered our the red-sequence sample.

6.2. Effects of Structural Evolution on the FP Zero-point Evolution

6.2.1. Zero-point Evolution and Luminosity Evolution

Following Saglia et al. (2010a, 2016), we can write the evolution of the FP zero-point in a generalized form including the terms related to the structural and stellar velocity dispersion evolution as well as the term describing the variation of the luminosity with redshift. Thus, the luminosity variation can be written as

$$\Delta \log L_{\mathrm{FP,str.ev.}} = \frac{2b+1}{b}\Delta \log R_{\mathrm{e}} - \frac{a}{b}\Delta \log \sigma_{\mathrm{e}} - \frac{1}{b}\Delta c_z, \tag{3}$$

where a and b are the FP coefficients from Equation (1). We parametrize each term of Equation (3) as a function of $\log(1+z)$ such that $\Delta \log R_{\mathrm{e}} = \nu \log(1+z)$, $\Delta \log \sigma_{\mathrm{e}} = \mu \log(1+z)$, and $\Delta c_z = \eta' \log(1+z)$, where ν, μ are the slopes of the size and stellar velocity dispersion evolutions with redshift, while η' is related to the slope we derive from the $\Delta \log M/L$ evolution with redshift; from Equation (2) $\eta' = \eta \times b$.

Equation (3) can therefore be written as

$$\begin{aligned}\Delta \log L_{\mathrm{FP,str.ev.}} &= \left(\frac{2b+1}{b}\nu - \frac{a}{b}\mu - \frac{1}{b}\eta'\right)\log(1+z)\\ &= \chi \log(1+z),\end{aligned} \tag{4}$$

where $\chi = \left(\frac{2b+1}{b}\nu - \frac{a}{b}\mu - \frac{1}{b}\eta'\right)$.

We first assume that the FP evolution is only due to the M/L evolution with redshift as a result of an aging stellar population. This means that the two terms $\Delta \log R_{\mathrm{e}}$, $\Delta \log \sigma_{\mathrm{e}}$ in Equation (3) are zero and $\Delta \log L_{\mathrm{FP}} = -\frac{1}{b}\eta' \log(1+z) = -\eta \log(1+z)$. Table 3, case (1), shows the results of the fit.

We then include in the luminosity evolution the effect of varying structural properties with redshift in the evolution of the FP; this means including all terms of Equation (4), and propagating the errors consistently.

6.2.2. Size–Mass and Stellar Velocity Dispersion–Mass Relations

We study how the size–mass and stellar velocity dispersion–mass relations vary with redshift for our “dispersion” sample adopting the Coma data as local reference, and by considering both stellar masses and dynamical masses (see Figure 7). For both relations we assume that the slope does not change with redshift and adopt the value we obtain from our Coma sample, as done in previous work (e.g., Saglia et al. 2010a; Newman et al. 2012). Chan et al. (2016) and Chan et al. (2017) present a more detailed analysis of the size–mass relation for the full

Table 3
Luminosity Evolution as Derived from the FP Zero-point with and without Structural Evolution, and from the Luminosity–Mass Relation

Case	Relation	XMM2235		XMM2215		Cl0332	
		$M_\star$	$M_{\rm dyn}$	$M_\star$	$M_{\rm dyn}$	$M_\star$	$M_{\rm dyn}$
1	$\Delta\log L_{\rm FP} = -\frac{1}{b}\eta'\log(1+z)$	1.68 ± 0.37		1.91 ± 0.25		2.10 ± 0.37	
2	$\Delta\log L_{\rm FP,str.ev.} = \chi\log(1+z)$[a]	1.01 ± 0.41	1.56 ± 0.48	1.25 ± 0.31	1.79 ± 0.39	1.44 ± 0.42	1.99 ± 0.48
3	$\Delta\log L_{L\text{-mass}} = \tau\log(1+z)$[a]	1.44 ± 0.12	1.72 ± 0.26	1.18 ± 0.22	1.97 ± 0.21	1.07 ± 0.14	2.04 ± 0.26

Note. The evolution of the galaxy luminosity as derived from the FP $L_{\rm FP}$, luminosity evolution including both structural evolution and FP zero-point evolution as described in Equation (4) $L_{\rm FP,str.ev.}$, and luminosity evolution from the mass–luminosity relation $L_{L\text{-mass}}$.

[a] To allow enough dynamic range to fit the size–mass, stellar velocity dispersion–mass and luminosity–mass relation, we adopt the full sample with $\log M_\star/M_\odot > 10.5$. Results are consistent within the errors if we trace the evolution of the luminosity only for the $\log M_\star/M_\odot > 11$ sample.

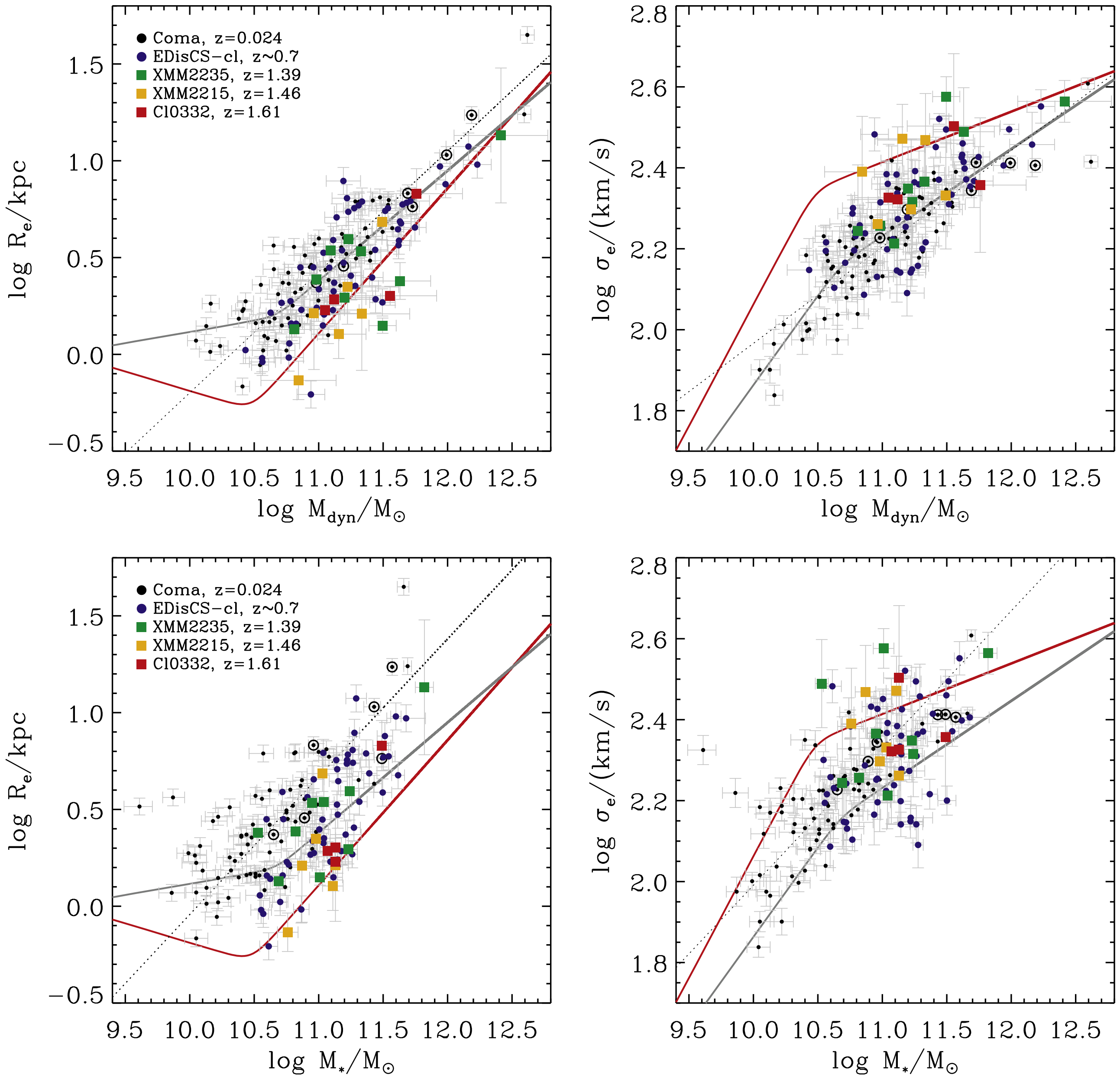

Figure 7. Left panels: size–mass relation. Right panels: stellar velocity dispersion–mass relation. Upper panels: dynamical masses are used. Lower panels: stellar masses are used. Symbols are the same as in Figure 5. Linear fits to the local data of Coma are shown with the dotted black lines; for comparison, we overplot the R_e–M and σ_e–M relations from Equation (5) of Cappellari et al. (2013a) with the gray solid line. In red we show the zone of exclusion for local galaxies from Equation (4) of Cappellari et al. (2013a) and Cappellari (2016).

red-sequence sample of the three clusters and confirm this assumption.

We note that the $R_{\rm e}$–$M_\star$ and $\sigma_{\rm e}$–$M_\star$ relations are part of a trend of size and stellar velocity dispersion with age and morphology (see Figure 1 of Cappellari et al. 2013a and Figure 20–23 of Cappellari 2016), and when this was not accounted for, different sample selections could be mistaken for structural evolution. For this reason, we also include in Figure 7 the zone of exclusion for local galaxies from Cappellari et al. (2013a) and Cappellari (2016); this region corresponds to a lower limit for the existence of local passive galaxies in the diagrams. For the left panels of Figure 7 we derive the zone of exclusion using Equation (4) of Cappellari et al. (2013a), and rescale the size along the semimajor axis given by that equation to a circularized size—as used in this work—adopting the median axis ratio of our Coma sample (∼0.65). For the right plots of Figure 7 we convert the zone of exclusion using the virial relation $M = 5.0 \times \sigma_{\rm e}^2 R_{\rm e}/G$ following the prescriptions of Cappellari et al. (2013a) and Cappellari (2016). We also overplot the $R_{\rm e}$–M and $\sigma_{\rm e}$–M relations from Equation (5) of Cappellari et al. (2013a) for comparison with our sample.

We note that the $R_{\rm e}-M_\star$ and $\sigma_{\rm e}-M_\star$ we find from our sample when adopting dynamical masses (black dotted lines in the upper panels of Figure 7) are consistent with those of Cappellari et al. (2013a) (gray solid lines in Figure 7) in the range of $M_{\rm dyn} > 10.67$. In this case, we also see that the sample of galaxies with the oldest ages in Coma are closer to the zone of exclusion, as expected based on the results of Cappellari (2016); about half of our KCS sample is either below or above the zone of exclusion defined by the $R_{\rm e} - M$ and $\sigma_{\rm e}$–M trends, respectively, as expected in the case of significant size evolution. When we adopt stellar masses, we see a zero-point offset in our fitted relation compared to that of Cappellari et al. (2013a), probably due to a ∼0.3 dex offset between dynamical and stellar masses in the Coma sample (see also Section 4). This offset could be due to effects of non-homology, or to a change of the IMF or dark matter fractions; understanding this offset is beyond the scope of this paper. For this reason, we test local scaling relations using both dynamical and stellar masses in our work.

To study the evolution of the scaling relations with redshift, we use the approach followed by Newman et al. (2012), Cimatti et al. (2012), Delaye et al. (2014), van der Wel et al. (2014), and Chan et al. (2017), where we remove the correlation between $R_{\rm e}$ and $M_\star$ (or $M_{\rm dyn}$) or $\sigma_{\rm e}$ and $M_\star$ (or $M_{\rm dyn}$) by dividing sizes and stellar velocity dispersions by a reference mass of $M \sim 10^{11}\,M_\odot$. We then trace the resulting quantities, which we call mass-normalized size $\log R_{\rm e,mass\text{-}norm}$ and stellar velocity dispersion $\log \sigma_{\rm e,mass\text{-}norm}$, as a function of redshift. This step is necessary when comparing samples with different mass distributions. After we assume the slope of the size–mass and stellar velocity dispersion–mass relation (see above), this procedure is equivalent to tracing the evolution of the zero-point of the $R_{\rm e}$ and $M_\star$ or $\sigma_{\rm e}$ and $M_\star$ relations.

Table 4
Redshift Evolution of $R_{\rm e}$ and $\sigma_{\rm e}$

Relation	$M_\star$-normalized slope	$M_{\rm dyn}$-normalized slope
$\Delta \log R_{\rm e,mass\text{-}norm} \propto \nu \log(1+z)$	-1.04 ± 0.12	-0.85 ± 0.30
$\Delta \log \sigma_{\rm e,mass\text{-}norm} \propto \mu \log(1+z)$	0.09 ± 0.10	0.34 ± 0.12

Note. Uncertainties on each parameter are 1σ jackknife errors. The evolution of $R_{\rm e}$ and $\sigma_{\rm e}$ is calculated for the three clusters simultaneously as $\Delta \log R_{\rm e,mass-norm} \propto \nu \log(1+z)$ and $\Delta \log \sigma_{\rm e,mass-norm} \propto \mu \log(1+z)$, respectively.

We trace the variation as a function of redshift of $\Delta \log R_{\rm e,mass\text{-}norm} \propto \nu \log(1+z)$ and $\Delta \log \sigma_{\rm e,mass\text{-}norm} \propto \mu \log(1+z)$ and derive the slopes ν and μ. The results for both stellar mass and dynamical-mass-normalized quantities are shown in Table 4. We fit the three KCS clusters together because the variations with redshift of $R_{\rm e}$ and $\sigma_{\rm e}$ have similar dynamic ranges for the three clusters; moreover, we include the full sample with $\log M_\star/M_\odot > 10.5$ in the fit. We note that the van der Wel et al. (2014) evolution of the median sizes in our mass bin in the field is slightly steeper than what we find in this work, possibly related to differences between cluster and field sample (see also Chan et al. 2017).

Median $R_{\rm e,mass\text{-}norm}$ for the three clusters are 55% smaller than median $R_{\rm e,mass\text{-}norm}$ of Coma galaxies when stellar-mass-normalized sizes are used, and 38% smaller when dynamical-mass-normalized radii are used. The median $\sigma_{\rm e,mass\text{-}norm}$ in the KCS sample is 3% larger than the median $\sigma_{\rm e,mass\text{-}norm}$ of Coma when stellar-mass-normalized quantities are used, and 20% larger when using dynamical-mass-normalized stellar velocity dispersions. This does not change when we use the subsample of Coma galaxies whose age is >9 Gyr: there is a 5%–7% difference between the median $R_{\rm e}$ of the whole Coma sample and the subsample with an age >9 Gyr; the difference reaches up to 20% for the median stellar velocity dispersions.

KCS galaxies follow a similar structural and stellar velocity dispersion evolution as the EDisCS-cluster sample (Saglia et al. 2010a). Our results for the size evolution partly disagree with a recent work by Jørgensen et al. (2014), where almost no size variation with redshift is found from their sample of clusters at $z < 1$ (from e.g., Jørgensen & Chiboucas 2013); their cluster at $z > 1.27$ shows trends similar to ours, suggesting that larger effects of size-evolution can be seen at $z > 1$. We note that the difference with the cluster sample at $z < 1$ could also be related to the different selections used in our sample and the sample of Jørgensen et al. (2014).

6.2.3. Effects of Structural Evolution on Derived Ages

The net contribution of structural and stellar velocity dispersion evolution $\chi_{\rm str-ev} = \left(\frac{2b+1}{b}\nu - \frac{a}{b}\mu\right)$ is -0.67 and -0.12 (a mean ∼35% and 6% of the FP zero-point evolution for our sample) when we consider relations of stellar mass or dynamical mass-normalized, respectively. $\chi_{\rm str-ev}$ is smaller than the η in case (1) of Table 3, suggesting that most of the zero-point evolution is indeed driven by the evolution of the luminosity. As mentioned above, the structural evolution we derive with stellar mass-normalized quantities is larger, which also affects the slopes in case (2) of Table 3, where we find shallower slopes.

We test the effect on the derived ages by rescaling up the $\Delta \log M/L$ of each overdensity by an amount corresponding to the percentage difference between the slopes of case (1) and case (2) of Table 3. Using the mass-normalized slopes of case (2), we find that the mean age of the $\log M_\star/M_\odot > 11$ galaxies in XMM2235 becomes larger than the age of the universe, which is unfeasible. We therefore consider as upper limit the age of the universe, which is a factor ~2 higher than the age we derive without considering structural evolution. For XMM2215, we find that the mean age becomes a factor ~2.4 larger, and for Cl0332 we find as well a mean age a factor ~2.4 larger than that we obtained when we do not include structural evolution in our analysis (case 1). The old ages we find suggest that the structural evolution we estimate using stellar-mass-normalized R_e and σ_e could be overestimated. This could be due to a stronger "progenitor bias" when selecting galaxies in $M_\star$, for instance. The sample of Coma galaxies for which we could compare the R_e and σ_e distributions for the oldest population is limited (i.e., only six galaxies have an age >9 Gyr); a larger sample of ages for Coma galaxies would be helpful to solve this issue.

By adopting the dynamical-mass-normalized slopes of case (2), we find older ages—although consistent within the errors—compared to those resulting from case (1). For XMM2235, the mean age becomes ~0.44 Gyr older, for XMM2215, it becomes ~ 0.22 Gyr older, and for Cl0332, it becomes ~ 0.18 Gyr older than the case in which structural evolution is not accounted for.

6.2.4. Luminosity Evolution from the Luminosity–Mass Relation

As an additional test, we compare the luminosity evolution derived from fitting the luminosity–mass relation as a function of redshift. For this we assume a constant slope of the luminosity–mass relation as derived from fitting the Coma sample. We follow a procedure similar to the size and stellar velocity dispersion, and derive both stellar mass and dynamical-mass-normalized luminosities, adopting $M \sim 10^{11}\,M_\odot$ as reference mass. We note that while fitting the luminosity–mass relation, we include the full sample with $\log M_\star/M_\odot > 10.5$ in the fit to allow a wide enough dynamic range. As expected, the results do not change using only galaxies with $\log M_\star/M_\odot > 11$ because we normalize the luminosity. This test is described by case (3) of Table 3, where $\Delta \log L_{L\text{-mass}} = \tau \log(1+z)$. Error bars are estimated with a jackknife technique. The results would not change if we were to use the sample of galaxies with age >9 Gyr rather than the full sample of Coma galaxies as reference. The difference of the median luminosity of the full sample and the sample with ages >9 Gyr is 19% for stellar-mass-normalized luminosities and 1% for dynamical-mass-normalized luminosities.

The three scenarios show consistent results when adopting dynamical-mass-normalized quantities, with an in general steeper luminosity evolution at constant dynamical mass, confirming the limited impact of structural evolution on our sample (see also Saglia et al. 2010a, 2016). We note that the use of stellar-mass-normalized quantities results in shallower slopes that (see the slope for Cl0332 in case (3) of Table 3) are inconsistent with the results from the FP zero-point.

6.3. Cluster Versus Field Comparison

The current findings show that massive $\log M_\star/M_\odot > 11$ galaxies in the three KCS overdensities have overall formation ages consistent within the errors. There is a possible weak suggestion that galaxies in the massive and virialized cluster XMM2235 are older than the massive galaxies in the lower density structure of Cl0332 after accounting for the difference in the age of the universe at the redshifts of the two overdensities. Similar results are found by fitting stellar population models to the stacked KMOS spectra (e.g., R. C. W. Houghton et al., 2017, in preparation).

Mendel et al. (2015) found an age of $1.03^{+0.13}_{-0.08}$ Gyr from the analysis of stacked spectra of a sample of passive galaxies at the median redshift of $\langle z \rangle = 1.75$, part of the KMOS VIRIAL field survey. The "redder" part of their sample at $\langle z \rangle = 1.73$ shows ages of $1.22^{+0.56}_{-0.19}$ Gyr, while the "bluer" part of their sample at $\langle z \rangle = 1.82$ is as young as $0.85^{+0.08}_{-0.05}$ Gyr. We compare our KCS sample with the field sample of VIRIAL by accounting for the difference between the redshift of the two samples.[13] Galaxies in Cl0332 show an average age that is consistent with the average age of massive galaxies in the full VIRIAL sample, which is expected because Cl0332 is by far the lowest density environment in our survey. For XMM2235, we find consistent mean ages with the "redder" VIRIAL population. XMM2235 ages are also consistent with the ages of the "blue" VIRIAL population, but with lower significance. This could originate from an accelerated evolution of galaxies in the most massive overdensities compared to field galaxies, as found in some FP studies at lower redshifts.

Saglia et al. (2010a) found a difference of about ~1 Gyr from the $\Delta \log M/L_B$ evolution of cluster and field galaxies from the EDisCS survey at $z \sim 0.7$, while Gebhardt et al. (2003) find a difference of ~2 Gyr for a sample of cluster and field galaxies at $z \sim 0.8$. By comparing $\Delta \log M/L_B$ of cluster and field galaxies up to $z \sim 1.27$, van Dokkum & van der Marel (2007) found an age difference of ~0.4 ± 0.2 Gyr, which is more in line with our findings. One of the possible sources of discrepancy between different studies could be the amount of progenitor bias in the field sample at $z > 1$ (e.g., Mendel et al. 2015), which could affect the cluster and field comparison (e.g., van Dokkum & van der Marel 2007). Our findings could be consistent with a scenario in which there is a link between the time of assembly of a cluster and the stellar population of the galaxies residing in it. Semi-analytical models, for instance, De Lucia et al. (2006), show an age difference of ~0.7 Gyr between massive galaxies in overdense and underdense regions of the universe.

By also including galaxies down to $\log M_\star/M_\odot = 10.5$ in the XMM2235 sample, we find younger ages, supporting previous findings of trends of age with $M_\star$(e.g., Treu et al. 2005; Renzini 2006; van der Marel & van Dokkum 2007). For XMM2215, the age does not change appreciably, which is probably related to some bias in the sample for which we derived stellar velocity dispersions.

6.4. Comparison with the Literature

Our results for XMM2235 are consistent with the results reported by Rosati et al. (2009), who inferred the ages of passive galaxies in the core and in the outskirts of this cluster by analyzing spectrophotometric data available from VLT/FORS2 and *HST*. They found that massive galaxies in the core of the cluster were formed at a formation redshift $z_f > 3$–4 (we find a formation redshift $z_f \sim 3$ for galaxies with $\log M_\star/M_\odot > 11$). Similarly, we agree with Lidman et al. (2008) and Strazzullo et al. (2010), who found formation redshifts $z_f > 3$ using both mean colors and scatter of the red sequence and luminosity function, respectively. We note also that our sample shows two main concentrations in the

---

[13] We note that Mendel et al. (2015) used Conroy et al. (2009) SSPs to derive their ages from stacked spectra. In Appendix C we show that if we were to use different SSPs in our FP analysis, ages would change by at most ~0.15 Gyr.

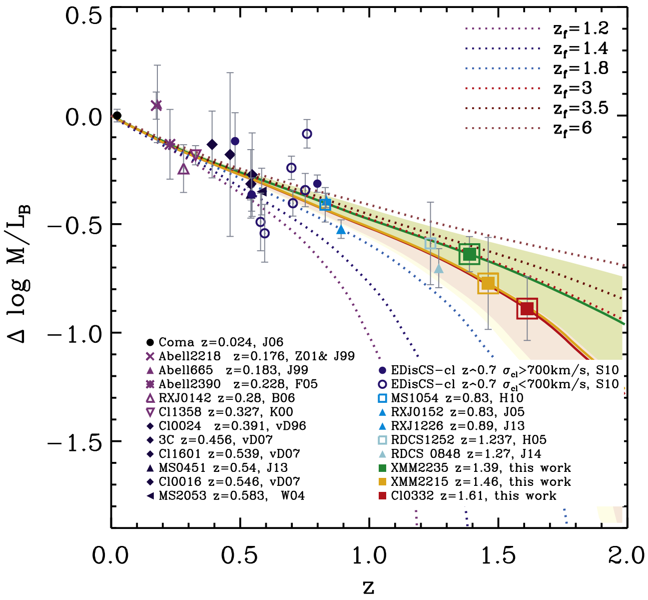

Figure 8. Redshift evolution of the weighted mean $\Delta \log M/L_B$ for the $\log M_\star/M_\odot > 11$ galaxies in each KCS cluster and for the $\log M_\star/M_\odot > 11$ galaxies in clusters in the literature. Symbols and lines are the same as in Figure 6 for the sample described in this paper. The literature sample is as follows: Coma, black filled circle (Jørgensen et al. 2006); Abell 2218, purple cross, derived by averaging the values from Jørgensen et al. (1999) and Ziegler et al. (2001); Abell 665, purple filled triangle (Jørgensen et al. 1999); Abell 2390, purple star (Fritz et al. 2005), RXJ0142, purple open triangle (Barr et al. 2005, 2006); Cl1358+62, purple open downward triangle (Kelson et al. 2000); Cl0024+16, navy filled diamond (van Dokkum & Franx 1996); 3C295, Cl1601+42, and Cl0016+16, navy filled diamonds (van Dokkum & van der Marel 2007); MS 0451.6-0305, navy filled triangle (Jørgensen & Chiboucas 2013); MS 2053-04, navy filled left-facing triangle (Wuyts et al. 2004); "EDisCS-cl" with a $\sigma_{\rm cl} > 700$ km s^{-1}, blue filled circles (Saglia et al. 2010a); "EDisCS-cl"' with a $\sigma_{\rm cl} < 700$ km s^{-1}, blue open circles (Saglia et al. 2010a); MS 1054-03, cyan empty square (Holden et al. 2010); RXJ0152-13, cyan filled triangle (Jørgensen et al. 2005); RXJ1226+33, cyan filled triangle (Jørgensen & Chiboucas 2013); RDCS1252.9-29, turquoise open square (Holden et al. 2005), RX J0848.6+44, turquoise filled triangle (Jørgensen et al. 2014).

$\Delta \log M/L_B - z$ plane, suggesting that there is probably an "older" and a "younger" population in the cluster.

Previous work on XMM2215 showed that galaxies in the cluster core have some level of star formation (e.g., Hilton et al. 2009, 2010; Hayashi et al. 2010, 2011; Ma et al. 2015; Hayashi et al. 2017; Stach et al. 2017). In our work we find that galaxies are on average slightly younger than the galaxies in XMM2235 (but still consistent within the errors), which could fit in a scenario in which for this cluster star formation is still ongoing while galaxies are falling into the denser cluster environment. However, we caution that this interpretation may not be valid given that for this cluster we derived a stellar velocity dispersion mostly in objects that are in the bluer part of the red sequence. The mean formation redshift $z_{\rm f} \sim 2.4$ for the galaxies in XMM2215 is consistent with the lower limit on the formation redshifts for the galaxies in the red sequence of the cluster found by Hilton et al. (2009) using the scatter and intercept of the CMD with respect to Coma.

The relatively young mean ages we derived for the galaxies in Cl0332 are in agreement with the ages found by Cimatti et al. (2008) and Kurk et al. (2009).

In Figure 8 we compare the weighted-mean $\Delta \log M/L_B$ evolution of the KCS sample with $\Delta \log M/L_B$ available in the literature for $\log M_\star/M_\odot > 11$ galaxies at $0.024 < z < 1.27$ in clusters with a wide range of mass and virialization status (see caption of Figure 8 for details). We homogenize photometric data from different samples to a common B-band surface brightness within the effective radius, following procedures similar to Appendix A of van Dokkum & van der Marel (2007). Error bars are uncertainties on the weighted mean. We find that our clusters extend up to $z = 1.61$ the trends we see at intermediate redshift, and expand the statistic in a redshift range currently almost unexplored. There are some weak hints that the most massive clusters have older formation redshifts, although errors are large and we cannot constrain these statements. We note, for instance, that our results for the $\log M_\star/M_\odot > 11$ galaxies in XMM2235 have formation redshifts on the order of the galaxies in the massive cluster RDCS1252.9-2927 at $z \sim 1.237$ (Holden et al. 2005). At intermediate redshift, we expect the differences to be more difficult to detect, and we indeed see a range of formation redshifts.

A larger number of clusters with different masses and properties at the same redshift we studied in this paper as well as at higher redshift will provide additional constraints to the scenario we described above.

7. Conclusions

In this paper we presented new results on the evolution of the FP of a sample of 19 passive galaxies in dense environments at $1.39 < z < 1.61$ from KCS, a GTO survey using KMOS at the VLT.

In the period between October 2013 to September 2016 KCS observed ⩾20 massive ($\log M_\star/M_\odot > 10.5$) passive galaxies in four main overdensities at $1.39 < z < 1.8$, with a range of masses and properties, as well as a lower-priority overdensity at $z = 1.04$ to bridge our high-redshift observations with the local sample. With KCS, we systematically targeted a large sample of galaxies in the red sequence and built a new sample of stellar velocity dispersions in *dense environments* at $z > 1.39$.

In this paper we presented the analysis of the KMOS data for the sample at $1.39 < z < 1.61$. KMOS data were combined with the structural parameters derived from *HST* imaging for the same galaxies, and we obtained the formation age through the FP.

Our main results can be summarized as follows:

1. The zero-point of the B-band FP evolves with redshift, such that the highest redshift cluster has the largest offset from Coma. By converting the zero-point evolution into an evolution of $\Delta \log M/L_B$ with redshift, we find that $\log M_\star/M_\odot > 11$ galaxies have $\Delta \log M/L_B = (-0.46 \pm 0.10)z$ in XMM2235 to $\Delta \log M/L_B = (-0.52 \pm 0.07)z$ in XMM2215, and $\Delta \log M/L_B = (-0.55 \pm 0.10)z$ for Cl0332. The $\Delta \log M/L_B$ becomes steeper when we include less massive ($10.5 < \log M_\star/M_\odot < 11$) objects, suggesting a trend with mass of the $\Delta \log M/L_B$.
2. By using Maraston (2005) single stellar population models, we derived mean formation ages for the sample with $\log M_\star/M_\odot > 11$ from the $\Delta \log M/L_B$ evolution with redshift. We find the mean luminosity-weighted ages to be $2.33^{+0.86}_{-0.51}$ Gyr, $1.59^{+1.40}_{-0.62}$ Gyr, and $1.20^{+1.03}_{-0.47}$ Gyr for XMM2235, XMM2215, and Cl0332, respectively. When we include in the sample of XMM2235 objects with $10.5 < \log M_\star/M_\odot < 11$, we derive younger ages

$\sim 1.63^{+0.39}_{-0.29}$ Gyr, suggesting a trend of age with $M_\star$. For XMM2215, we obtain consistent ages of $\sim 1.62^{+1.30}_{-0.61}$ Gyr.

3. Our results are robust against the use of different SSPs or metallicity assumptions. Formation ages are also consistent with the expectation for the color evolution from SSPs.
4. Effects of structural and stellar velocity dispersion evolution are responsible for ∼6%–35% of the evolution we see in the FP zero-point, most of which instead comes from the M/L evolution. The net impact of structural and stellar velocity dispersion evolution on the measurements of the galaxy ages is ∼2–2.4 Gyr when we consider structural evolution and velocity dispersion evolution normalized by the stellar mass (i.e., 35% contribution in the FP zero-point evolution). Ages vary at most by ∼0.44 Gyr for XMM2235 when using structural evolution and velocity dispersion evolution normalized by the dynamical mass; for XMM2215 and Cl0332, the variation is smaller. When we fit the luminosity–mass relation, we find a similar evolution of the luminosity with redshift to the evolution we find in the FP.
5. The mean $\Delta \log M/L_B$ of the galaxies in the three overdensities relative to Coma are consistent with passive evolution with formation ages consistent within the errors for the three clusters. However, there is a weak suggestion that more massive and virialized clusters are formed at earlier times compared with galaxies in a lower-density structure in our sample. This is consistent with our findings from the stellar population analysis of stacked KMOS spectra of the same galaxies, as discussed in a companion paper (e.g., R. C. W. Houghton et al., 2017, in preparation). We also find that massive $\log M_\star/M_\odot > 11$ galaxies in XMM2235 have ages consistent with the "red" population of passive galaxies in the field at similar redshift from the VIRIAL KMOS GTO survey. XMM2235 ages are also consistent with the ages of the "blue" VIRIAL population, but with a lower significance.

We thank the entire KMOS instrument and commissioning teams for their hard work, which has allowed our observing program to be carried out successfully. We wish to thank the ESO staff, and in particular the staff at the Paranal Observatory, for their support during the observing runs over which the KMOS GTO observations were carried out. We acknowledge the anonymous referee for valuable comments that led to an improved presentation. We thank Matt Hilton for the reduced MOIRCS imaging, and Greg Rudnick for providing the updated catalog of stellar masses for EDisCS galaxies prior publication. A.B. thanks Paola Santini for providing the CANDELS GOODS-S catalogs of stellar masses for comparisons prior to appearance on the public website. A.B. acknowledges Claudia Maraston and Janine Pforr for the stellar mass catalog of SDSS/DR7 galaxies. We would also like to thank Chris Lidman for providing HAWK-I images of XMMXCS J2215-1738 for the construction of our wide field-of-view photometry catalogs. J.C.C.C. acknowledges the support of the Deutsche Zentrum für Luft- und Raumfahrt (DLR) via Project ID 50OR1513. D.J.W. acknowledges the support of the Deutsche Forschungsgemeinschaft via Project ID 3871/1-1 and ID 3871/1-2. This work was supported by the UK Science and Technology Facilities Council through the "Astrophysics at Oxford" grant ST/K00106X/1. R.L.D. acknowledges travel and computer grants from Christ Church, Oxford and support from the Oxford Centre for Astrophysical Surveys which is funded by the Hintze Family Charitable Foundation. M.C. acknowledges support from a Royal Society University Research Fellowship. J.P.S gratefully acknowledges support from a Hintze Research Fellowship. R.J.S. was supported by the STFC through grant ST/L00075X/1. This research has made use of the SVO Filter Profile Service (http://svo2.cab.inta-csic.es/theory/fps/) supported by the Spanish MINECO through grant AyA2014-55216.

Appendix A
Derivation of the Kinematics from Different Parts of the Spectrum

We assess the robustness of our fits by measuring the stellar velocity dispersion separately in the blue and red parts of our spectra. This is done for the clusters XMM2235 and XMM2215, where multiple diagnostic lines are available in regions free from telluric absorption or strong sky emission. The blue part of the spectrum covers mostly the *G*-band and H_γ, and also the Ca line for XMM2215, while the red part includes mostly the H_β and Fe lines, and Mg for XMM2235. We note that the S/N significantly decreases in the blue part of the spectrum because of the lower throughput of KMOS in the bluer part of the *YJ* band, which affects the uncertainties of our measurements. Moreover, the blue part of the spectrum we fit covers a shorter wavelength range than the red part. This could potentially affect the set of templates applied by the fitting procedure. To circumvent this issue, we adopt the same combination of templates derived in the fit of the full spectrum in both the fit of the blue and red part. As discussed in Section 3.3, before performing the kinematic fit, we smooth the KMOS spectrum with a variable kernel to a common FWHM to match the maximum FWHM. This should prevent us from adding systematics related to the KMOS resolution in the blue and red part of the spectrum.

Figure 9 shows a comparison of the results obtained by fitting the full spectrum and the blue part (left panels), the full spectrum and the red part (central panels), and red and blue part (right panels). The actual value is determined as the mode of the distribution over the 100 bootstrap realizations and the error as the standard deviation. The actual value of the stellar velocity dispersion from our spectra is consistent within the errors with the mode of the distribution of σ_e derived from the bootstrap realizations.

For XMM2235, we find that the kinematics derived from the blue part and from the full spectrum have a median difference $\Delta\sigma = -37.50$ km s^{-1} ($\Delta \log \sigma = -0.08$) and a 1σ scatter of 70.11 km s^{-1}, while by fitting the red region of the spectrum, we find an offset $\Delta\sigma = -35.55$ km s^{-1} ($\Delta \log \sigma = -0.06$) and a 1σ scatter of 56.20 km s^{-1} from the fit of the full spectrum. The median difference between the fit of the blue and red part of the spectrum is $\Delta\sigma = 16.41$ km s^{-1} ($\Delta \log \sigma = 0.04$) with a 1σ scatter of 72.54 km s^{-1}. In XMM2235 the quality of some data in the "blue" part is particularly poor, resulting in a few objects with systematically higher σ_e than in the full sample.

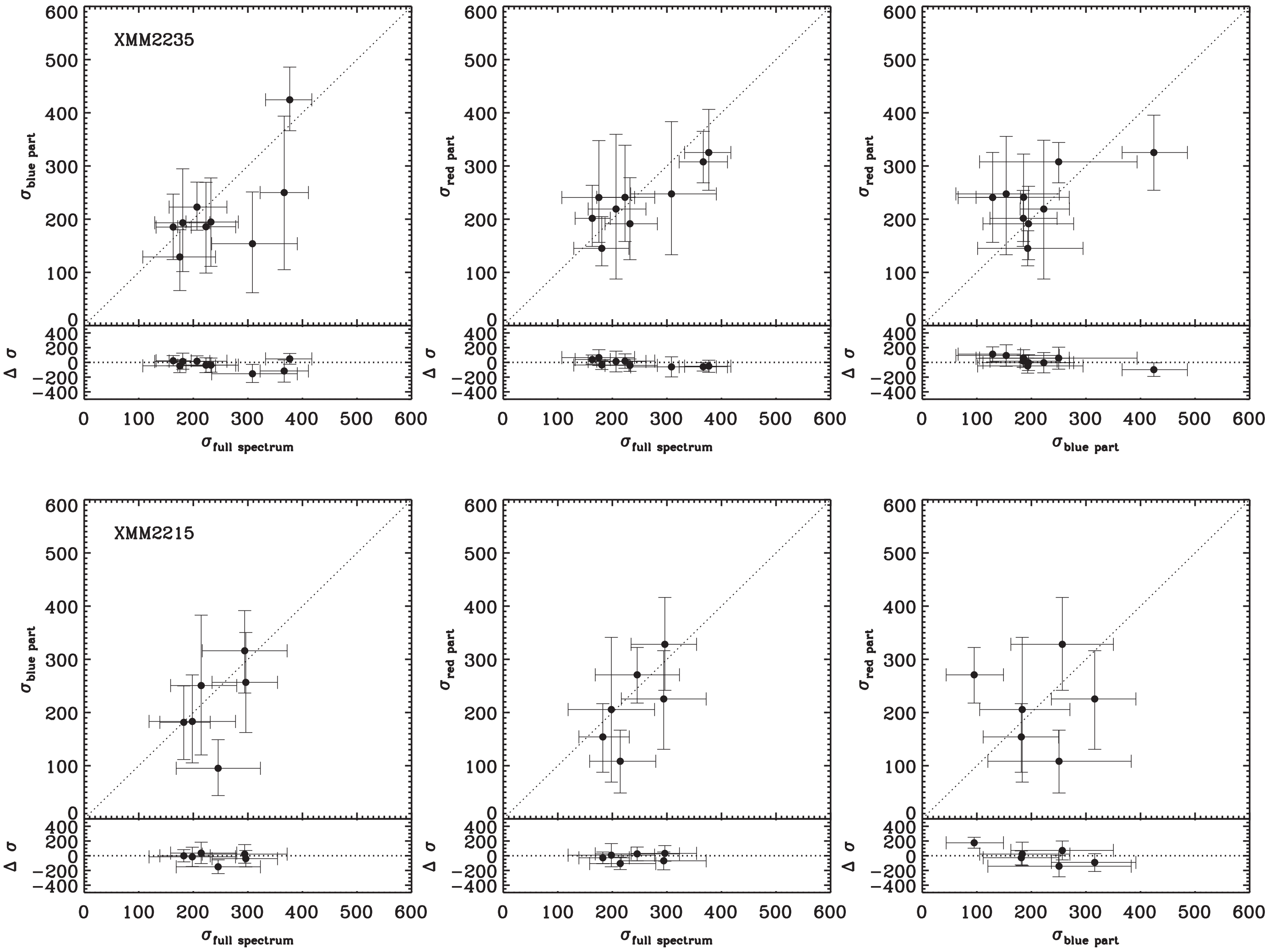

Figure 9. Comparison between the stellar velocity dispersion measurements in the blue and red part of the spectrum for XMM2235 (upper panel) and XMM2215 (lower panel). From left to right, the panels show the comparison between the fit in the full spectrum and the blue part, the full spectrum and the red part, and between blue and red part, respectively.

For XMM2215, we find that the kinematics derived from the blue part and from the full spectrum have a median difference $\Delta\sigma = -7.99$ km s^{-1} ($\Delta \log \sigma = -0.02$) and a 1σ scatter of 60.80 km s^{-1}, while by fitting the red region of the spectrum, we find an offset of $\Delta\sigma = -10.53$ km s^{-1} ($\Delta \log \sigma = -0.03$) and a 1σ scatter of 60.00 km s^{-1} from the fit of the full spectrum. The median difference between the fit of the blue and red part of the spectrum is $\Delta\sigma = -2.54$ km s^{-1} ($\Delta \log \sigma = 0.01$) with a 1σ scatter of 121.41 km s^{-1}.

This test aims at assessing the systematic effect we can have from deriving stellar velocity dispersions from different absorption lines at different redshift. It did not result in a rejection of galaxies, which were mostly discarded at the stage of fitting the full spectrum through all the bootstrap realizations. Generally, the systematic offsets $\Delta \log \sigma_e$ between the full spectrum fit and the two subregions of the spectra are usually <10%, and smaller than the typical 10%–40% uncertainty we have from fitting the full spectrum. Single objects could potentially have larger offsets than the median value given above in one of the wavelength ranges, but this could be attributed to a poorer quality of the spectrum in that wavelength range.

Appendix B
Success Rate and Selection Functions

In this section we describe the technique used to assess the selection effects for the three overdensities in our sample. We derive selection weights by assigning a selection probability to each galaxy with a method similar to that used by Saglia et al. (2010a).

We first derive the completeness in measuring stellar velocity dispersion for each of the clusters in our sample. We split the red sequence of our CMDs into equally spaced magnitude bins (see Figure 2), and for each bin, we compute the ratio of the number of red-sequence galaxies with measured stellar velocity dispersion to the total number of galaxies in the red sequence in that bin. For the three overdensities, we use different combinations of magnitudes in the CMDs, therefore we derive separate weights for the three overdensities, based on the three different photometries. We assign a probability to each galaxy by linearly interpolating these selection curves. As we could expect, the stellar velocity dispersion completeness is larger at brighter magnitudes.

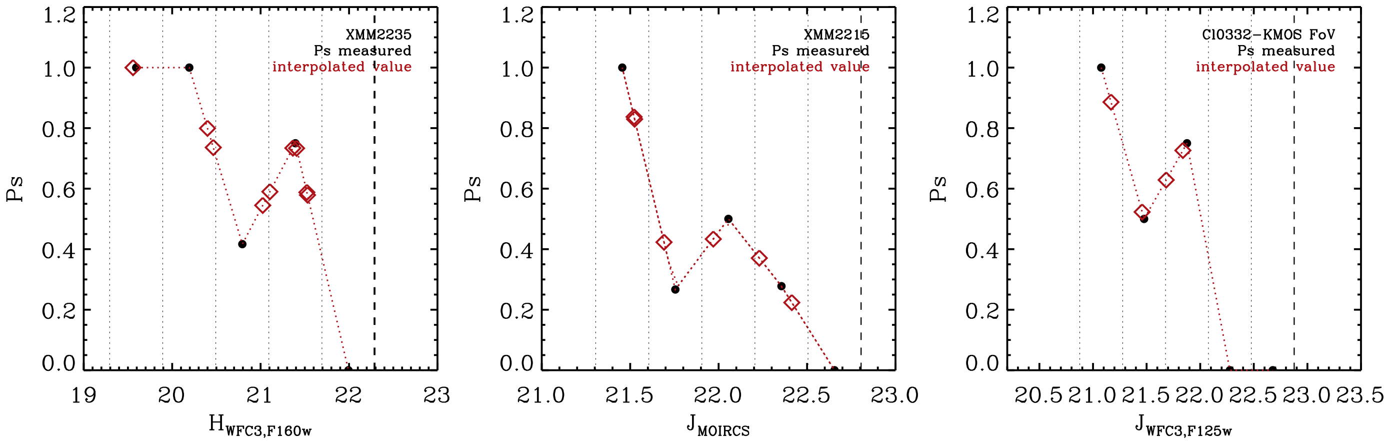

Figure 10. Completeness functions P_S of our cluster galaxies showing how many objects in the red sequence of our clusters have measured stellar velocity dispersions, normalized by how many objects were spectroscopically found to be members of the clusters over those allocated in the red sequence. Black circles show the average quantities per bin, and red diamonds show the interpolated values corresponding to the magnitudes of the galaxies in our sample. Vertical dotted lines show the magnitude bins used to evaluate the selection functions for our sample (see also Figure 2). From left to right, we show the functions for XMM2235, XMM2215, and Cl0332.

We then rescale this fraction by the ratio between the number of objects found to be spectroscopically confirmed members of the cluster over the number of galaxies we targeted with KMOS for each magnitude bin in the CMD; these represent our selection weights P_s.

We note that for XMM2235, where we targeted 83% of the objects in the red sequence with $H_{\rm F160w} < 22.3$, we find that half of the objects at $21.7 < H_{\rm F160w} < 22.3$ are either background or foreground objects, confirming our expectations from the statistical analysis in Section 2.3.2. Our findings also support the results of Chan et al. (2017), who reached the same conclusions using two-color diagrams.

Figure 10 shows the weights as a function of the selection magnitude, which is used for each cluster in Figure 2. The dashed lines show our limiting magnitude for the KMOS observations of the three clusters, and the dotted lines show the magnitude bins as already shown in Figure 2. Black dots are the average points used to derive the curves, and the red lines and diamonds show the interpolated values at the magnitude of each galaxy. For Cl0332, we derive weights for both the subsample of galaxies within the region of the overdensity described by the field of view of our KMOS pointing (see Figure 10) and for all the objects within ±3000 km s^{-1} of the overdensity redshift extending over the whole GOODS-S field. In the latter case, we find similar weights for the two brightest bins, and lower weights for the third magnitude bin because there are more objects in the red sequence. The completeness in the velocity dispersion measurement for Cl0332 is higher at bright magnitudes and decreases toward fainter objects. The trend is less clear for XMM2215, which we observed for a similar exposure time.

We test whether the weights correlate with galaxy properties. XMM2235 does not show strong correlations, while for XMM2215 and Cl0332, the weights tend to be higher for more luminous and more massive objects.

Appendix C
Effect of Using Different Stellar Population Models and Metallicity Assumptions

van Dokkum & van der Marel (2007) (their Figure 7) already showed that the evolution of the $\Delta \log M/L_B$ for an SSP is similar in Maraston (2005) and Bruzual & Charlot (2003) SSPs in the age range between 9 and 10 Gyr in B band. In this section we assess whether this is still valid in the redshift range of our overdensities.

We generate M/L in the B band as a function or redshift and formation redshift using the `EzGal` code of Mancone & Gonzalez (2012) for both the Bruzual & Charlot (2003) SSPs and the Conroy et al. (2009) and Conroy & Gunn (2010) SSPs with solar metallicity. We also produce M/L for the Bruzual & Charlot (2003) SSPs with super-solar metallicities of $[{\rm Fe/H}] \sim 0.56$ and sub-solar metallicity of $[{\rm Fe/H}] \sim -0.33$. As is known, the Bruzual & Charlot (2003) SSPs and the Conroy et al. (2009) and Conroy & Gunn (2010) SSPs give similar $\Delta \log M/L_B$ with redshift, and give a negligible difference in the fitted parameters, therefore in the following we quote only results based on Bruzual & Charlot (2003).

We repeat the analysis described in Section 6.1 by minimizing the difference between $\Delta \log M/L_B$ of the Bruzual & Charlot (2003) SSPs with different formation redshifts (or age) and the $\Delta \log M/L_B$ of our KCS sample with $\log M_\star/M_\odot > 11$. Ages differ by at most 0.15 Gyr between using Maraston (2005) and Bruzual & Charlot (2003) SSPs in the B band. As expected, this difference decreases with increasing formation redshift, when the models give almost the same result.

We find consistent formation redshifts when we traced the color evolution of galaxies with redshift using Bruzual & Charlot (2003) SSPs.

Our original assumption about the solar metallicity does not change our results either within the errors. By adopting Bruzual & Charlot (2003) SSPs with super-solar metallicities of $[{\rm Fe/H}] \sim 0.56$ (but assuming solar metallicity at redshift 0 based on the known values of metallicity for Coma), the mean ages would become at most ~0.6 Gyr younger than with solar metallicity, while in case of sub-solar metallicity of $[{\rm Fe/H}] \sim -0.33$ (and assuming solar metallicity at redshift 0), we derive ages that are at most ~1 Gyr older.

In summary, our results are robust against the use of different SSPs and different metallicity assumptions, and we maintain the same trends we see using solar metallicity Maraston (2005) SSPs.

ORCID iDs

Alessandra Beifiori https://orcid.org/0000-0001-8017-6097
J. Trevor Mendel https://orcid.org/0000-0002-6327-9147
Jeffrey C. C. Chan https://orcid.org/0000-0001-6251-3125
Roberto P. Saglia https://orcid.org/0000-0003-0378-7032
Ralf Bender https://orcid.org/0000-0001-7179-0626
Michele Cappellari https://orcid.org/0000-0002-1283-8420
David J. Wilman https://orcid.org/0000-0002-1822-4462

References

Andreon, S., Newman, A. B., Trinchieri, G., et al. 2014, A&A, 565, A120
Barden, M., Häußler, B., Peng, C. Y., McIntosh, D. H., & Guo, Y. 2012, MNRAS, 422, 449
Barr, J., Davies, R., Jørgensen, I., Bergmann, M., & Crampton, D. 2005, AJ, 130, 445
Barr, J., Jørgensen, I., Chiboucas, K., Davies, R., & Bergmann, M. 2006, ApJL, 649, L1
Bauer, A. E., Grützbauch, R., Jørgensen, I., Varela, J., & Bergmann, M. 2011, MNRAS, 411, 2009
Beifiori, A., Maraston, C., Thomas, D., & Johansson, J. 2011, A&A, 531, A109
Beifiori, A., Thomas, D., Maraston, C., et al. 2014, ApJ, 789, 92
Bell, E. F., & de Jong, R. S. 2001, ApJ, 550, 212
Bell, E. F., McIntosh, D. H., Katz, N., & Weinberg, M. D. 2003, ApJS, 149, 289
Belli, S., Newman, A. B., & Ellis, R. S. 2014a, ApJ, 783, 117
Belli, S., Newman, A. B., & Ellis, R. S. 2015, ApJ, 799, 206
Belli, S., Newman, A. B., & Ellis, R. S. 2017, ApJ, 834, 18
Belli, S., Newman, A. B., Ellis, R. S., & Konidaris, N. P. 2014b, ApJL, 788, L29
Bender, R. 1990, A&A, 229, 441
Bender, R., Burstein, D., & Faber, S. M. 1992, ApJ, 399, 462
Bender, R., Saglia, R. P., & Gerhard, O. E. 1994, MNRAS, 269, 785
Bender, R., Saglia, R. P., Ziegler, B., et al. 1998, ApJ, 493, 529
Bertin, E., & Arnouts, S. 1996, A&AS, 117, 393
Bezanson, R., van Dokkum, P. G., van de Sande, J., et al. 2013, ApJL, 779, L21
Blanton, M. R., & Roweis, S. 2007, AJ, 133, 734
Bleem, L. E., Stalder, B., de Haan, T., et al. 2015, ApJS, 216, 27
Brammer, G. B., van Dokkum, P. G., Franx, M., et al. 2012, ApJS, 200, 13
Brammer, G. B., Whitaker, K. E., van Dokkum, P. G., et al. 2011, ApJ, 739, 24
Bruzual, G., & Charlot, S. 2003, MNRAS, 344, 1000
Bullock, J. S., Kolatt, T. S., Sigad, Y., et al. 2001, MNRAS, 321, 559
Cappellari, M. 2013, ApJL, 778, L2
Cappellari, M. 2016, ARA&A, 54, 597
Cappellari, M. 2017, MNRAS, 466, 798
Cappellari, M., Bacon, R., Bureau, M., et al. 2006, MNRAS, 366, 1126
Cappellari, M., di Serego Alighieri, S., Cimatti, A., et al. 2009, ApJL, 704 L34
Cappellari, M., & Emsellem, E. 2004, PASP, 116, 138
Cappellari, M., McDermid, R. M., Alatalo, K., et al. 2013a, MNRAS, 432, 1862
Cappellari, M., Scott, N., Alatalo, K., et al. 2013b, MNRAS, 432, 1709
Carlberg, R. G., Yee, H. K. C., & Ellingson, E. 1997, ApJ, 478, 462
Carollo, C. M., Cibinel, A., Lilly, S. J., et al. 2013, ApJ, 776, 71
Castellano, M., Salimbeni, S., Trevese, D., et al. 2007, ApJ, 671, 1497
Cenarro, A. J., & Trujillo, I. 2009, ApJL, 696, L43
Chabrier, G. 2003, PASP, 115, 763
Chan, J. C. C., Beifiori, A., Mendel, J. T., et al. 2016, MNRAS, 458, 3181
Chan, J. C. C., Beifiori, A., Saglia, R. P., et al. ApJ, 2017, submitted
Cimatti, A., Cassata, P., Pozzetti, L., et al. 2008, A&A, 482, 21
Cimatti, A., Nipoti, C., & Cassata, P. 2012, MNRAS, 422, L62
Conroy, C., & Gunn, J. E. 2010, ApJ, 712, 833
Conroy, C., Gunn, J. E., & White, M. 2009, ApJ, 699, 486
Correa, C. A., Wyithe, J. S. B., Schaye, J., & Duffy, A. R. 2015a, MNRAS, 450, 1514
Correa, C. A., Wyithe, J. S. B., Schaye, J., & Duffy, A. R. . 2015b, MNRAS, 450, 1521
Correa, C. A., Wyithe, J. S. B., Schaye, J., & Duffy, A. R. 2015c, MNRAS, 452, 1217
Davies, R. I., Agudo Berbel, A., Wiezorrek, E., et al. 2013, A&A, 558 A56
Davies, R. L., Beifiori, A., Bender, R., et al. 2015, in IAU Symp. 311, Galaxy Masses as Constraints of Formation Models, ed. M. Cappellari & S. Courteau (Cambridge: Cambridge Univ. Press), 110
De Lucia, G., Springel, V., White, S. D. M., Croton, D., & Kauffmann, G. 2006, MNRAS, 366, 499
Delaye, L., Huertas-Company, M., Mei, S., et al. 2014, MNRAS, 441, 203
di Serego Alighieri, S., Lanzoni, B., & Jørgensen, I. 2006, ApJL, 647, L99
di Serego Alighieri, S., Vernet, J., Cimatti, A., et al. 2005, A&A, 442, 125
Djorgovski, S., & Davis, M. 1987, ApJ, 313, 59
Dressler, A., Lynden-Bell, D., Burstein, D., et al. 1987, ApJ, 313, 42
Faber, S. M., Dressler, A., Davies, R. L., Burstein, D., & Lynden-Bell, D. 1987, in Nearly Normal Galaxies. From the Planck Time to the Present, ed. S. M. Faber (New York: Springer-Verlag), 175
Fagioli, M., Carollo, C. M., Renzini, A., et al. 2016, ApJ, 831, 173
Finoguenov, A., Tanaka, M., Cooper, M., et al. 2015, A&A, 576, A130
Fritz, A., Ziegler, B. L., Bower, R. G., Smail, I., & Davies, R. L. 2005, MNRAS, 358, 233
Gebhardt, K., Faber, S. M., Koo, D. C., et al. 2003, ApJ, 597, 239
Giavalisco, M., Ferguson, H. C., Koekemoer, A. M., et al. 2004, ApJL, 600, L93
Gonzaga, S., Hack, W., Fruchter, A., & Mack, J. 2012, The DrizzlePac Handbook (Baltimore, MD: STScI)
Grogin, N. A., Kocevski, D. D., Faber, S. M., et al. 2011, ApJS, 197, 35
Grützbauch, R., Bauer, A. E., Jørgensen, I., & Varela, J. 2012, MNRAS, 423, 3652
Guo, Y., Ferguson, H. C., Giavalisco, M., et al. 2013, ApJS, 207, 24
Hayashi, M., Kodama, T., Kohno, K., et al. 2017, ApJL, 841, L21
Hayashi, M., Kodama, T., Koyama, Y., et al. 2010, MNRAS, 402, 1980
Hayashi, M., Kodama, T., Koyama, Y., et al. 2014, MNRAS, 439, 2571
Hayashi, M., Kodama, T., Koyama, Y., Tadaki, K.-I., & Tanaka, I. 2011, MNRAS, 415, 2670
Hill, A. R., Muzzin, A., Franx, M., & van de Sande, J. 2016, ApJ, 819, 74
Hilton, M., Collins, C. A., Stanford, S. A., et al. 2007, ApJ, 670, 1000
Hilton, M., Lloyd-Davies, E., Stanford, S. A., et al. 2010, ApJ, 718, 133
Hilton, M., Stanford, S. A., Stott, J. P., et al. 2009, ApJ, 697, 436
Hogg, D. W., Baldry, I. K., Blanton, M. R., & Eisenstein, D. J. 2002, arXiv:astro-ph/0210394
Holden, B. P., Illingworth, G. D., Franx, M., et al. 2007, ApJ, 670, 190
Holden, B. P., van der Wel, A., Franx, M., et al. 2005, ApJL, 620, L83
Holden, B. P., van der Wel, A., Kelson, D. D., Franx, M., & Illingworth, G. D. 2010, ApJ, 724, 714
Horne, K. 1986, PASP, 98, 609
Houghton, R. C. W., Davies, R. L., Dalla Bontà, E., & Masters, R. 2012, MNRAS, 423, 256
Houghton, R. C. W., Davies, R. L., D'Eugenio, F., et al. 2013, MNRAS, 436, 19
Hu, W., & Kravtsov, A. V. 2003, ApJ, 584, 702
Huertas-Company, M., Shankar, F., Mei, S., et al. 2013, ApJ, 779, 29
Jee, M. J., Dawson, K. S., Hoekstra, H., et al. 2011, ApJ, 737, 59
Jørgensen, I. 1999, MNRAS, 306, 607
Jørgensen, I., Bergmann, M., Davies, R., et al. 2005, AJ, 129, 1249
Jørgensen, I., & Chiboucas, K. 2013, AJ, 145, 77
Jørgensen, I., Chiboucas, K., Flint, K., et al. 2006, ApJL, 639, L9
Jørgensen, I., Chiboucas, K., Toft, S., et al. 2014, AJ, 148, 117
Jørgensen, I., Franx, M., Hjorth, J., & van Dokkum, P. G. 1999, MNRAS, 308, 833
Jørgensen, I., Franx, M., & Kjaergaard, P. 1995, MNRAS, 276, 1341
Jørgensen, I., Franx, M., & Kjaergaard, P. 1996, MNRAS, 280, 167
Kausch, W., Noll, S., Smette, A., et al. 2014, in ASP Conf. Ser. 485, Astronomical Data Analysis Software and Systems XXIII, ed. N. Manset & P. Forshay (San Francisco, CA: ASP), 403
Kelson, D. D., Illingworth, G. D., van Dokkum, P. G., & Franx, M. 2000, ApJ, 531, 184
Koekemoer, A. M., Faber, S. M., Ferguson, H. C., et al. 2011, ApJS, 197, 36
Kroupa, P. 2001, MNRAS, 322, 231
Kurk, J., Cimatti, A., Daddi, E., et al. 2013, A&A, 549, A63
Kurk, J., Cimatti, A., Zamorani, G., et al. 2009, A&A, 504, 331
Lani, C., Almaini, O., Hartley, W. G., et al. 2013, MNRAS, 435, 207
Lidman, C., Iacobuta, G., Bauer, A. E., et al. 2013, MNRAS, 433, 825
Lidman, C., Rosati, P., Tanaka, M., et al. 2008, A&A, 489, 981
Łokas, E. L., & Mamon, G. A. 2003, MNRAS, 343, 401
Ma, C.-J., Smail, I., Swinbank, A. M., et al. 2015, ApJ, 806, 257
Mancone, C. L., & Gonzalez, A. H. 2012, PASP, 124, 606
Maraston, C. 2005, MNRAS, 362, 799
Maraston, C., Pforr, J., Henriques, B. M., et al. 2013, MNRAS, 435 2764

Maraston, C., & Strömbäck, G. 2011, MNRAS, 418, 2785
Maraston, C., Strömbäck, G., Thomas, D., Wake, D. A., & Nichol, R. C. 2009, MNRAS, 394, L107
Markwardt, C. B. 2009, in ASP Conf. Ser. 411, Astronomical Data Analysis Software and Systems XVIII, ed. D. A. Bohlender, D. Durand, & P. Dowler (San Francisco, CA: ASP), 251
Mendel, J. T., Saglia, R. P., Bender, R., et al. 2015, ApJL, 804, L4
Mendel, J. T., Simard, L., Palmer, M., Ellison, S. L., & Patton, D. R. 2014, ApJS, 210, 3
Meyers, J., Aldering, G., Barbary, K., et al. 2012, ApJ, 750, 1
Milvang-Jensen, B., Noll, S., Halliday, C., et al. 2008, A&A, 482, 419
Momcheva, I. G., Brammer, G. B., van Dokkum, P. G., et al. 2016, ApJS, 225, 27
Moustakas, J., Coil, A. L., Aird, J., et al. 2013, ApJ, 767, 50
Mullis, C. R., Rosati, P., Lamer, G., et al. 2005, ApJL, 623, L85
Muzzin, A., Marchesini, D., Stefanon, M., et al. 2013, ApJ, 777, 18
Newman, A. B., Belli, S., & Ellis, R. S. 2015, ApJL, 813, L7
Newman, A. B., Ellis, R. S., Andreon, S., et al. 2014, ApJ, 788, 51
Newman, A. B., Ellis, R. S., Bundy, K., & Treu, T. 2012, ApJ, 746, 162
Oke, J. B., & Gunn, J. E. 1983, ApJ, 266, 713
Oke, J. B., & Sandage, A. 1968, ApJ, 154, 21
Papovich, C., Finkelstein, S. L., Ferguson, H. C., Lotz, J. M., & Giavalisco, M. 2011, MNRAS, 412, 1123
Patel, S. G., van Dokkum, P. G., Franx, M., et al. 2013, ApJ, 766, 15
Peng, C. Y., Ho, L. C., Impey, C. D., & Rix, H.-W. 2010, AJ, 139, 2097
Pforr, J., Maraston, C., & Tonini, C. 2012, MNRAS, 422, 3285
Piffaretti, R., Arnaud, M., Pratt, G. W., Pointecouteau, E., & Melin, J.-B. 2011, A&A, 534, A109
Planck Collaboration, Ade, P. A. R., Aghanim, N., et al. 2016, A&A, 594, A27
Poggianti, B. M., Moretti, A., Calvi, R., et al. 2013, ApJ, 777, 125
Prugniel, P., & Soubiran, C. 2001, yCat, 3218, 0
Prugniel, P., Soubiran, C., Koleva, M., & Le Borgne, D. 2007, yCat, 3251, 0
Renzini, A. 2006, ARA&A, 44, 141
Renzini, A., & Ciotti, L. 1993, ApJL, 416, L49
Rosati, P., Tozzi, P., Gobat, R., et al. 2009, A&A, 508, 583
Saglia, R. P., Fabricius, M., Bender, R., et al. 2010b, A&A, 509, A61
Saglia, R. P., Sánchez-Blázquez, P., Bender, R., et al. 2016, A&A, 596, C1
Saglia, R. P., Sánchez-Blázquez, P., & Bender, R. E. A. 2010a, A&A, 524, A6
Salpeter, E. E. 1955, ApJ, 121, 161
Sánchez-Blázquez, P., Jablonka, P., Noll, S., et al. 2009, A&A, 499, 47
Sánchez-Blázquez, P., Peletier, R. F., Jiménez-Vicente, J., et al. 2006, MNRAS, 371, 703
Santini, P., Ferguson, H. C., Fontana, A., et al. 2015, ApJ, 801, 97
Saracco, P., Casati, A., Gargiulo, A., et al. 2014, A&A, 567, A94
Schlafly, E. F., & Finkbeiner, D. P. 2011, ApJ, 737, 103
Scholz, F. W., & Stephens, M. A. 1987, J. Am. Stat. Assoc., 82, 918
Scott, N., Fogarty, L. M. R., Owers, M. S., et al. 2015, MNRAS, 451, 2723
Sérsic, J. L. 1968, Atlas de Galaxias Australes (Cordoba, Argentina: Observatorio Astronomico)
Sharples, R., Bender, R., Agudo Berbel, A., et al. 2012, Proc. SPIE, 8446, 0
Sharples, R., Bender, R., Agudo Berbel, A., et al. 2014, Proc. SPIE, 9147, 0
Shetty, S., & Cappellari, M. 2015, MNRAS, 454, 1332
Simard, L., Clowe, D., Desai, V., et al. 2009, A&A, 508, 1141
Skelton, R. E., Whitaker, K. E., Momcheva, I. G., et al. 2014, ApJS, 214, 24
Stach, S. M., Swinbank, A. M., Smail, I., Hilton, M., & Simpson, J. M. 2017, arXiv:1705.03479
Stanford, S. A., Romer, A. K., Sabirli, K., et al. 2006, ApJL, 646, L13
Stott, J. P., Collins, C. A., Sahlén, M., et al. 2010, ApJ, 718, 23
Strazzullo, V., Gobat, R., Daddi, E., et al. 2013, ApJ, 772, 118
Strazzullo, V., Rosati, P., Pannella, M., et al. 2010, A&A, 524, A17
Tanaka, M., Toft, S., Marchesini, D., et al. 2013, ApJ, 772, 113
Thomas, D., Maraston, C., Bender, R., & Mendes de Oliveira, C. 2005, ApJ, 621, 673
Thomas, D., Maraston, C., Schawinski, K., Sarzi, M., & Silk, J. 2010, MNRAS, 404, 1775
Thomas, J., Saglia, R. P., Bender, R., et al. 2007, MNRAS, 382, 657
Tinsley, B. M., & Gunn, J. E. 1976, ApJ, 203, 52
Toft, S., Gallazzi, A., Zirm, A., et al. 2012, ApJ, 754, 3
Treu, T., Ellis, R. S., Liao, T. X., & van Dokkum, P. G. 2005, ApJL, 622, L5
Trujillo, I., Conselice, C. J., Bundy, K., et al. 2007, MNRAS, 382, 109
Valentinuzzi, T., Fritz, J., Poggianti, B. M., et al. 2010, ApJ, 712, 226
van de Sande, J., Kriek, M., Franx, M., et al. 2011, ApJL, 736, L9
van de Sande, J., Kriek, M., Franx, M., et al. 2013, ApJ, 771, 85
van de Sande, J., Kriek, M., Franx, M., Bezanson, R., & van Dokkum, P. G. 2014, ApJL, 793, L31
van der Marel, R. P., & van Dokkum, P. G. 2007, ApJ, 668, 756
van der Wel, A., Franx, M., van Dokkum, P. G., et al. 2005, ApJ, 631, 145
van der Wel, A., Franx, M., van Dokkum, P. G., et al. 2014, ApJ, 788, 28
van Dokkum, P. G., & Franx, M. 1996, MNRAS, 281, 985
van Dokkum, P. G., & Franx, M. 2001, ApJ, 553, 90
van Dokkum, P. G., Franx, M., Kelson, D. D., & Illingworth, G. D. 1998, ApJL, 504, L17
van Dokkum, P. G., Kriek, M., & Franx, M. 2009, Natur, 460, 717
van Dokkum, P. G., Leja, J., Nelson, E. J., et al. 2013, ApJL, 771, L35
van Dokkum, P. G., & Stanford, S. A. 2003, ApJ, 585, 78
van Dokkum, P. G., & van der Marel, R. P. 2007, ApJ, 655, 30
Wegner, M., & Muschielok, B. 2008, Proc. SPIE, 7019, 70190T
Whitaker, K. E., Labbé, I., van Dokkum, P. G., et al. 2011, ApJ, 735, 86
Williams, M. J., Bureau, M., & Cappellari, M. 2010, MNRAS, 409 1330
Wuyts, S., van Dokkum, P. G., Kelson, D. D., Franx, M., & Illingworth, G. D. 2004, ApJ, 605, 677
Ziegler, B. L., Bower, R. G., Smail, I., Davies, R. L., & Lee, D. 2001, MNRAS, 325, 1571